



저작자표시-비영리-변경금지 2.0 대한민국

이용자는 아래의 조건을 따르는 경우에 한하여 자유롭게

- 이 저작물을 복제, 배포, 전송, 전시, 공연 및 방송할 수 있습니다.

다음과 같은 조건을 따라야 합니다:



저작자표시. 귀하는 원저작자를 표시하여야 합니다.



비영리. 귀하는 이 저작물을 영리 목적으로 이용할 수 없습니다.



변경금지. 귀하는 이 저작물을 개작, 변형 또는 가공할 수 없습니다.

- 귀하는, 이 저작물의 재이용이나 배포의 경우, 이 저작물에 적용된 이용허락조건을 명확하게 나타내어야 합니다.
- 저작권자로부터 별도의 허가를 받으면 이러한 조건들은 적용되지 않습니다.

저작권법에 따른 이용자의 권리는 위의 내용에 의하여 영향을 받지 않습니다.

이것은 [이용허락규약\(Legal Code\)](#)을 이해하기 쉽게 요약한 것입니다.

[Disclaimer](#)

공학박사 학위논문

**Laplace-domain waveform
inversion using a single damping
constant**

단일 감쇠상수를 이용한
라플라스 영역 완전파형역산

2015 년 8 월

서울대학교 대학원

에너지시스템공학부

신 정 균

Laplace-domain waveform inversion using a single damping constant

지도 교수 신 창 수

이 논문을 공학박사 학위논문으로 제출함
2015 년 5 월

서울대학교 대학원
에너지시스템공학부
신 정 균

신정균의 공학박사 학위논문을 인준함
2015 년 6 월

위 원 장 _____ (인)

부위원장 _____ (인)

위 원 _____ (인)

위 원 _____ (인)

위 원 _____ (인)

Abstract

Laplace-domain waveform inversion (LWI) produces long-wavelength velocity models of the earth by using the Laplace transformed wave field. LWI is recognized as an efficient method for building long-wavelength velocity models because real data, which lacks low frequency information, can be inverted with minimal pre-processing stages such as band-pass filtering and first-arrival picking. Originally, the LWI algorithm was developed for 2-D acoustic media, but it has recently been extended for more realistic environments, such as acoustic and elastic media with irregular topography and 3-D acoustic, elastic and acoustic-elastic coupled media. In addition, the computing efficiency is significantly enhanced by exploiting the explicit time-domain modeling algorithm or implicit Laplace-domain modeling using an iterative matrix solver. Conventional LWI using various damping constants produces promising results. However, there remain several issues to be addressed: (1) the role of each damping constant is not clearly identified, so the combination of the optimal damping constants is empirically decided without a theoretical background; (2) there has not been any study to assess the potential issues caused by extremely small and large damping constants; (3) conventionally used multiple damping constants make the LWI algorithm computationally intensive.

LWI using a single damping constant (single-damping LWI), which is the main topic of this study, is motivated by the similar appearances of the inversion results obtained from LWI using different damping constants. Through the numerical experiment, the trends of inverted velocity model using different damping constants are identified, and the potential issues caused by extremely small and large damping constants, when the time-domain seismic data are used, are analyzed. Using the result of numerical experiment, range of proper damping constant for single-damping LWI is suggested. By inverting the Laplace-domain wave field with respect to the selected representative damping constant, the computing efficiency is

dramatically enhanced (up to 6 times faster) while maintaining the quality of the inversion result (model misfit is smaller than 3). New scaling method using a depth weighting function is proposed in this study, and it provides the better convergence rate for single-damping LWI. Finally, real towed streamer data are used to verify the feasibility of single-damping LWI algorithm by comparing the result with that of the conventional LWI.

Keywords : Laplace-domain waveform inversion, full waveform inversion, single damping constant, depth weighting function

Student number : 2011-21101

Contents

1. Introduction.....	1
1.1. Laplace-domain waveform inversion	1
1.2. Issues in Laplace-domain waveform inversion	5
1.3. Laplace-domain waveform inversion using a single damping constant	7
2. Review of the Laplace-domain waveform inversion.....	8
2.1. Laplace-domain waveform modeling	9
2.2. Gradient direction for the logarithmic objective function	11
2.3. Pseudo Hessian for the logarithmic objective function	14
3. Laplace-domain waveform inversion using a single damping constant.....	17
3.1. Resemblance of gradient direction using different damping constants.....	21
3.2. Inversion results for different damping constants.....	29
3.3. Issues in the gradient direction using small and large damping constants.....	36
3.4. Range for proper damping constants for single-damping LWI	63
3.5. Accuracy of single-damping LWI using a depth weighting function	64
3.6. Computational efficiency of single-damping LWI	73
4. Real dataset example	78
4.1. Preprocessing for the Laplace-domain waveform inversion	79
4.2. Accuracy of the inverted velocity model.....	83
5. Conclusion	94
Reference	96
초록	101

List of Figures

Figure 1. Pluto 1.5 velocity model	19
Figure 2. Source wavelet for the time domain modeling	20
Figure 3. An example common shot gather when the source is located at 20 km of the velocity model	20
Figure 4. Pluto synthetic velocity model with a star marking the source location.....	25
Figure 5. Synthetic common shot gather in the time domain when the source is located at the star in Figure 4 and receivers are located over at the entire surface	25
Figure 6. Synthetic common shot gathers in the frequency domain for three discrete frequencies (1.25, 3.75, and 6.25 Hz).....	26
Figure 7. Synthetic common shot gathers in the Laplace domain for three damping constants (3, 7, and 11 s ⁻¹).....	26
Figure 8. Frequency-domain gradient direction using (a) 1.25, (b) 2.5, (c) 3.75, (d) 5, and (e) 6.25 Hz. (f) is a summed gradient using 24 frequencies between 1.25 and 7 Hz at an interval of 0.25 Hz.....	27
Figure 9. Laplace-domain gradient using (a) 3, (b) 5, (c) 7, (d) 9, and (e) 11 s ⁻¹ . (f) is a summed gradient using 7 damping constants between 1 and 13 s ⁻¹ at an interval of 2 s ⁻¹	28
Figure 10. The two-layered homogeneous velocity model for LWI	31
Figure 11. Inverted velocity model obtained by single-damping LWI using a damping constant of (a) 1, (b) 2, (c) 3, (d) 4, (e) 5, (f) 6, (g) 7, (h) 8, (i) 9, (j) 10, (k) 11, (l) 12, (m) 13, (n) 14, and (o) 15 s ⁻¹	32
Figure 12. Relative model misfit of the Laplace-domain inverted velocity model for different damping constants	35
Figure 13. Causal sinusoids having (a) infinite listening time and (b) finite listening time, and (c) the difference between (a) and (b). In these figures, A is 1, ω is 2π , T_{max} is 15.7, and T_f is 3.0.....	42
Figure 14. Example common shot gathers with maximum listening times of (a) 16, (b) 12, and (c) 8 s when the source is located at 20 km of the velocity model.....	43
Figure 15. Inverted velocity model obtained by single-damping LWI using a	

	damping constant of (a) 1, (b) 2, (c), 3, (d) 4, (e) 5, and (f) 6 s^{-1} for synthetic data with a maximum listening time of 16 s.....	44
Figure 16.	Inverted velocity model obtained by single-damping LWI using a damping constant of (a) 1, (b) 2, (c), 3, (d) 4, (e) 5, and (f) 6 s^{-1} for synthetic data with a maximum listening time of 12 s.....	45
Figure 17.	Inverted velocity model obtained by single-damping LWI using a damping constant of (a) 1, (b) 2, (c), 3, (d) 4, (e) 5, and (f) 6 s^{-1} for synthetic data with a maximum listening time of 8 s.....	46
Figure 18.	Time trace of the (a) noise-free observed data (d_{ideal}), (b) pure noise data (n), and (c) the noise-contaminated data ($d_{noisy}=d_{ideal}+n$). In this figure, T_d is equal to T_n assuming random noises.....	53
Figure 19.	An example common shot gather with random noise where the source is located at 20 km of the velocity model	54
Figure 20.	Comparison of the traces at 6km from Figure 18 with (red solid line) and without (black solid line) random noises	54
Figure 21.	Inverted velocity model obtained by single-damping LWI using a damping constant of (a) 1, (b) 2, (c), 3, (d) 4, (e) 5, and (f) 6 s^{-1} for synthetic data with random noises	55
Figure 22.	An example common shot gather with coherent noise where the source is located at 20 km of the velocity model	56
Figure 23.	Comparison of the traces at 6km from Figure 21 with (red solid line) and without (black solid line) coherent noises	56
Figure 24.	Inverted velocity model obtained by single-damping LWI using a damping constant of (a) 1, (b) 2, (c), 3, (d) 4, (e) 5, and (f) 6 s^{-1} for synthetic data with coherent noise	57
Figure 25.	Synthetic common shot gather in the Laplace domain for five large damping constants (7, 9, 11, 13, and 15 s^{-1}). The thick black solid line is the minimum value (10^{-38}) that can be represented in the single-precision waveform inversion program	62
Figure 26.	Diagrams for (a) conventional LWI using various damping constants and (b) proposed single-damping LWI using a scaling method with a depth weighting function.....	68
Figure 27.	Inverted velocity model obtained using conventional LWI	69
Figure 28.	Inverted velocity model obtained using single-damping with the depth weighting function using a damping constant of 7 s^{-1}	69

Figure 29. History of the relative model misfit between the inverted velocity model using conventional LWI and inverted velocity model using single-damping LWI regularized by pseudo Hessian only and regularized by pseudo Hessian and depth weighing using a damping constant of 7 s^{-1}	70
Figure 30. Inverted velocity models in the frequency domain using the (a) two-layered homogeneous and (b) linear gradient velocity models as the initial velocity model	71
Figure 31. Inverted velocity models in the frequency domain using the result of (a) conventional LWI and (b) single-damping LWI as an initial velocity model.....	72
Figure 32. Elapsed time for an iteration with respect to the total number of sources when the grid interval is (a) 25, (b) 50, and (c) 100 m using 7 CPU cores. The \times marks represent the elapsed time of conventional LWI, and the $+$ marks represent the elapsed time of single-damping LWI. The linear trend lines are plotted with black solid lines using 9 samples for all cases.....	76
Figure 33. Speedup of the proposed single-damping LWI algorithm compared to the conventional LWI algorithm using the linear trend lines calculated from the 9 discrete samples in Figure 31	77
Figure 34. An example common shot gather when the source is located 24 km of the imaging area.....	81
Figure 35. Frequency spectrum of the example common shot gather.....	81
Figure 36. Laplace-domain common shot gather when the damping constant is (a) 3, (b) 7, and (c) 11 s^{-1} when the source is located 24 km of the imaging area.....	82
Figure 37. The two-layered homogeneous velocity model for Laplace-domain waveform inversion	86
Figure 38. Inverted velocity model obtained by the (a) conventional LWI using 7 damping constants from 1 to 13 s^{-1} at an interval of 2 s^{-1} , and (b) single-damping LWI with depth weighting function using a damping constant of 7 s^{-1}	86
Figure 39. Brute migrated image from the frequency-domain reverse time migration algorithm using the two-layered homogeneous velocity model	87
Figure 40. Migrated image from the frequency-domain reverse time migration algorithm using the result of (a) conventional LWI and (b) single-damping LWI	87

Figure 41. Comparison of the Laplace-domain observed and modeled data at the 301 st shot position using the conventional LWI result with damping constants of (a) 3, (b), 7, and (c), 11 s ⁻¹ . (d), (e), and (f) are the same comparison as (a), (b), and (c) using the single-damping LWI result	88
Figure 42. Comparison of the Laplace-domain observed and modeled data at the 601 st shot position using the conventional LWI result with damping constants of (a) 3, (b), 7, and (c), 11 s ⁻¹ . (d), (e), and (f) are the same comparison as (a), (b), and (c) using the single-damping LWI result	89
Figure 43. Comparison of the Laplace-domain observed and modeled data at the 901 st shot position using the conventional LWI result with damping constants of (a) 3, (b), 7, and (c), 11 s ⁻¹ . (d), (e), and (f) are the same comparison as (a), (b), and (c) using the single-damping LWI result	90
Figure 44. Time-domain (a) observed data and modeled data using the result of (b) conventional LWI and (c) single-damping LWI at the 301 st shot position	91
Figure 45. Time-domain (a) observed data and modeled data using the result of (b) conventional LWI and (c) single-damping LWI at the 601 st shot position	92
Figure 46. Time-domain (a) observed data and modeled data using the result of (b) conventional LWI and (c) single-damping LWI at the 901 st shot position	93

1. Introduction

1.1. Laplace-domain waveform inversion

Full waveform inversion (FWI) is a subsurface velocity estimation method that minimizes the difference between observed and modeled wave fields using automated computer simulation. Since Lailly (1983) and Tarantola (1984) suggested the adjoint-state method, which reduces computing costs consumed when calculating partial derivative wave fields, FWI has been widely studied by a number of geophysicists and applied mathematicians. The conventional FWI algorithms and their various applications are well described by Virieux and Operto (2009). In the early stages, most studies were performed in the time domain (Bunks et al., 1995; Mora, 1987; Shipp and Singh, 2002; Tarantola, 1986, 1984); to increase the computing efficiency for seismic data with many common shot gathers, frequency-domain waveform inversion has been suggested and studied (Operto et al., 2004; Pratt et al., 1998; Shin and Min, 2006; Shin et al., 2007).

Even though the conventional time- and frequency-domain waveform inversions are theoretically ideal methods for estimating the subsurface velocity by considering all types of waves (e.g., direct wave, reflected wave, refracted wave, diving wave, and multiples), they suffer from several limitations when they are applied to real data. Most FWI algorithms are implemented by numerical optimization algorithms based on local descent methods, such as the full Newton method, Gauss-Newton method, or steepest descent method. Because of the local minimum problem, which is caused by the nonlinearity of the wave equations, the solution of the conventional waveform inversion converges frequently to the wrong velocity model (local minimum), which is completely different from the true velocity model (global minimum). This behavior is true especially when the initial velocity model is not close to the true velocity model (Mora, 1987). The objective function for the low frequency component of the seismic signal has fewer local minima, but the low frequency components are still hardly obtained in the real data

using the current seismic acquisition techniques (Symes, 2008) despite several efforts at recording low-frequency data (Plessix and Baeten, 2010; Soubaras and Lafet, 2013). A good-quality initial velocity model can mitigate the local minimum problem, so various velocity estimation techniques yielding the long-wavelength features of the true subsurface geology are used to generate a good initial guess for the FWI. First arrival travel time tomography is the most common method for generating the long-wavelength velocity model (Toomey et al., 1994; Zelt and Barton, 1998). In addition to this method, migration velocity analysis (Symes and Carazzone, 1991; Yang and Sava, 2011; Yilmaz and Chambers, 1984) and stereotomography (Billette and Lambaré, 1998; Billette et al., 2003) can be used to estimate the initial model for FWI.

To overcome the limitations of conventional waveform inversion, Laplace-domain waveform inversion (LWI) was developed (Shin and Cha, 2008). Contrary to the conventional time- and frequency-domain waveform inversion, LWI is performed using Laplace-transformed seismic data with respect to various damping constants. The objective function in the Laplace domain shows a smoother surface and fewer local minima compared to that in the time or frequency domains (Shin and Ha, 2008). Therefore, the result of this process is barely affected by the quality of the initial velocity model, so very simple velocity models such as the linear gradient or homogeneous models can be used as good initial models. In addition, the frequency contents in seismic data modify only the scale of the Laplace-domain wave field, which can be compensated by the source estimation procedure; consequently, the lack of the low frequency component does not degrade the gradient direction in the Laplace domain (Ha and Shin, 2013). In contrast to the first arrival travel time tomography (which is the most commonly used method to produce the long-wavelength velocity model), LWI considers not only the first-arrived refracted waves but also the reflected waves that arrived later by solving the full (two-way) wave equation, and it enables enhancing the illumination depth (Bae et al., 2012). After LWI, Laplace-Fourier-domain waveform inversion and conventional frequency-domain waveform inversion

can be performed, and more detailed (medium to short wavelength) structures can be added to the smooth velocity model inverted in the Laplace domain (Kim et al., 2013; Shin and Cha, 2009; Shin et al., 2010).

Waveform inversion in the Laplace domain shares most parts of the computation algorithm with that in the frequency domain (Laplace-domain waveform modeling and inversion can be easily implemented by assigning pure imaginary values to the complex frequency variable of the frequency-domain waveform modeling and inversion algorithm). However, with respect to the computational efficiency, the Laplace domain shows a dramatic enhancement. The numerical dispersion, which is caused by the spatial discretization method, such as the finite difference method or the finite element method, is lower in the Laplace domain, and it has been analyzed in previous studies (Pyun et al., 2011; Shin and Cha, 2008). Therefore, a larger grid interval can be adopted, which leads to a smaller degree of the freedom of impedance matrix that is to be factorized and solved. Spurious reflections, which are observed when irregular elements with different sizes are used together, can also be suppressed in the Laplace domain (Shin et al., 2013). Moreover, it was proven that the sparse shot sampling does not degrade the quality of the inverted velocity model in the Laplace domain (Ha and Shin, 2012a), and the symmetric and positive definite property of the impedance matrix enable us to perform the 3-D waveform inversion using an iterative matrix solver (Pyun et al., 2011).

The LWI algorithm using the pure acoustic approximation (assuming the entire earth is only a fluid in which only the compressional wave field propagates) has produced several promising results for real marine data as well as synthetic marine data (Ha et al., 2012a; Koo et al., 2011; Shin et al., 2014). It also shows favorable applicability to both synthetic and real land data utilizing the fact that the effect of elastic waves, which can be regarded as noise in the acoustic approximation, is minimized in the Laplace domain due to the slow wave speed of shear and surface waves propagating in elastic

media (Ha et al., 2010b; Shin et al., 2013).

1.2. Issues in Laplace-domain waveform inversion

LWI solves various problems of conventional waveform inversion performed either in the time or frequency domain. Yet, there are still some issues that have not been solved. In this section, some unsolved issues in LWI will be discussed.

The biggest problem of LWI is the selection of the optimal damping constants for the Laplace transform of the time-domain wave field. Depending on the grouping of the damping constants, the inverted velocity model shows a different result. Until now, multiple damping constants ranging from 1 to 20 s^{-1} are commonly used simultaneously in many studies on LWI for acoustic media (Bae et al., 2012; Ha and Shin, 2012b; Ha et al., 2012a; Koo et al., 2011; Pyun et al., 2011; Shin et al., 2014). Through various numerical tests using synthetic and real data, the combination of the optimal damping constants have been empirically selected. Ha et al. (2010) and Ha et al. (2012) attempted to find the proper range of damping constants by defining the threshold in the floating point operation and analyzing the penetration depth of the Laplace-domain wave field, but it does not give us a clear answer for selecting optimal damping constants. In addition, the role of different damping constants has not been clearly explained, and the potential risk caused by specific damping constants is not identified.

Second, the Laplace transformation that is applied to the time domain seismic data is not theoretically perfect. In LWI, the modeled wave field can be implicitly calculated using the Laplace-transformed wave equation to achieve efficient computation for multi-source modeling (Marfurt, 1984; Shin and Cha, 2008). In contrast, Laplace-domain observed wave field, which are to be compared with the Laplace-domain modeled wave field, is obtained by the discrete Laplace transform of the time-domain observed data. Theoretically, seismic data, which is to be transformed into the Laplace domain, should be defined from 0 to positive infinity. However, seismic data

always have limited listening times, which hinders the ideal Laplace transformation of the time-domain seismic data.

Third, the effect of various noises can be significant. Any type of signal that cannot be simulated using the governing wave equation is regarded as noise in the waveform inversion algorithm. Seismic data always suffers from different type of noise (e.g., random noise, coherent noise, instrumental noise, 3-D effects, and elastic effects). The Laplace transform can be interpreted as the summation of the amplitude of exponentially damped seismic signals using certain damping constant. Therefore, when seismic data containing noise is transformed into the Laplace domain, the negative effects of the early-arrival noise events are maximized (Ha et al., 2012a). First arrival picking is essentially performed to mute the noisy events that arrive before the first arrival, but it does not alleviate the effects caused by the noises that arrived after the first arrival signals.

Fourth is the computational cost. LWI requires fewer computing resources compared to the frequency-domain waveform inversion for various reasons that are explained in section 1.1. However, irrespective of the occurrence of numerical dispersions and spurious reflections, using an extremely coarse grid interval, such as several hundred meters, can be a matter of describing an exact acquisition geometry (position of the source and receiver) or geological feature on the sea bottom or topography of elastic media. In addition, 3-D seismic acquisition is becoming more common, and solving the 3-D wave equation requires overwhelmingly larger computational resources compared to its 2-D counterpart. An iterative matrix solver or explicit time-domain modeling can be an alternative method for reducing the memory consumption when solving the huge impedance matrix, but it loses the most important benefit of implicit Laplace-domain wave equation modeling; the high efficiency of multi-source modeling.

1.3. Laplace-domain waveform inversion using a single damping constant

In this study, I suggest LWI using only a single damping constant (single-damping LWI). By inverting the wave field for one of the representative damping constants among various candidates that are used by conventional LWI, the computing efficiency can be enhanced while maintaining the quality of the inverted velocity model. In addition, a new scaling method using the depth weighting function is suggested for enhancing the quality of the inverted velocity model obtained by the single-damping LWI algorithm.

2. Review of the Laplace-domain waveform inversion

In this section, I briefly review the meaning of Laplace-domain wave field and conventional Laplace-domain waveform modeling and inversion algorithm.

2.1. Laplace-domain waveform modeling

When $u(t)$ is a time-domain seismic signal, the Laplace-transformed seismic signal $\tilde{u}(s)$ for damping constant s can be defined as follows:

$$\tilde{u}(s) = \int_0^{\infty} u(t)e^{-st} dt. \quad (1)$$

To investigate the meaning of the Laplace transform of the time domain seismic signal using the conventional frequency-domain point of view, Equation 1 can be rewritten with the extended interval of the definite integral using the causality of the time domain seismic signal ($u(t) = 0$ for $t < 0$) and the concept of angular frequency ω :

$$\tilde{u}(s) = \lim_{\omega \rightarrow 0} \int_{-\infty}^{\infty} u(t)e^{-st} e^{-i\omega t} dt. \quad (2)$$

In Equation 2, we can immediately see that $\tilde{u}(s)$ corresponds to the zero-frequency component of exponentially damped seismic signals. This zero frequency component enables the reconstruction of the long-wavelength velocity model. In addition, the optimized selection of the Laplace damping constant is necessary for enhancing the illumination depth (Shin and Cha, 2008).

Instead of applying the Laplace transform to the time-domain signal, we can simulate the Laplace-transformed wave field $\tilde{u}(\mathbf{x}, s)$ using the Laplace-domain acoustic wave equation directly:

$$\nabla^2 \tilde{u}(\mathbf{x}, s) - \frac{s^2}{c^2} \tilde{u}(\mathbf{x}, s) = \tilde{f}(\mathbf{x}, s), \quad (3)$$

where c is the speed of the compressional wave field propagation in the acoustic media, s is the damping constant, \mathbf{x} is spatial index, and $\tilde{f}(\mathbf{x}, s)$ is

the source wavelet in the Laplace domain.

Through the discretization using the standard finite element method, Equation 3 can be converted into a matrix-vector form as follows:

$$\mathbf{S}\tilde{\mathbf{u}} = \tilde{\mathbf{f}},$$
$$\mathbf{S} = \mathbf{M}s^2 + \mathbf{K} \quad (4)$$

where \mathbf{S} is the impedance matrix, \mathbf{M} is the mass matrix, \mathbf{K} is the stiffness matrix, and $\tilde{\mathbf{u}}$ and $\tilde{\mathbf{f}}$ are vectors for the Laplace-domain wave field and source wavelet, respectively. However, the detailed discretization process for the acoustic media is outside the scope of this study. Finally, the Laplace-domain wave field $\tilde{\mathbf{u}}$, can be obtained by inverting matrix \mathbf{S} using the matrix solver.

2.2. Gradient direction for the logarithmic objective function

In the waveform inversion algorithm based on the steepest descent method, the velocity is iteratively updated using the gradient direction of the objective function to minimize the difference between the observed and modeled wave field. In the Laplace domain, the numerical solution of the wave equation has an extremely small value, especially for receivers that are far from the source position. Therefore, the differences at all of the receivers cannot be considered properly using the conventional l_2 objective function. Therefore, the l_2 objective function for the logarithmic wave field is regarded as an effective approach for a rapidly decaying wave field in the Laplace domain, and it is called the logarithmic objective function (Shin and Cha, 2008; Shin and Min, 2006).

The l_2 objective function for the logarithmic wave field, which is commonly referred to as the logarithmic objective function, can be defined as

$$E(\mathbf{m}) = \frac{1}{2} \sum_{i=1}^{n_s} \sum_{j=1}^{n_r} (\log(\tilde{u}_{ij}(\mathbf{m})) - \log(\tilde{d}_{ij}))^2, \quad (5)$$

where \tilde{u}_{ij} and \tilde{d}_{ij} are the Laplace-domain modeled and observed wave fields, respectively, at the j -th receiver caused by the i -th source; n_s and n_r are the total number of sources and receivers, respectively; and \mathbf{m} is the model parameter vector standing for the velocity of the compressional wave in the acoustic media.

The partial derivative of Equation 5 with respect to the k -th model parameter can be calculated as

$$\frac{\partial E(\mathbf{m})}{\partial m_k} = \sum_{i=1}^{n_s} \sum_{j=1}^{n_r} \frac{\partial \tilde{u}_{ij}(\mathbf{m})}{\partial m_k} \left(\frac{\log(\tilde{u}_{ij}(\mathbf{m})/\tilde{d}_{ij})}{\tilde{u}_{ij}(\mathbf{m})} \right). \quad (6)$$

Using the adjoint-state method (Plessix, 2006; Pratt et al., 1998), Equation 6 can be obtained without explicitly calculating the partial derivative wave field $\frac{\partial u_{ij}(\mathbf{m})}{\partial m_k}$ using the concept of a virtual source vector \mathbf{v}_{m_k}

$$\frac{\partial E(\mathbf{m})}{\partial m_k} = \sum_{i=1}^{n_s} (\mathbf{v}_{m_k})^T \mathbf{S}^{-1} \mathbf{r}_i, \quad (7)$$

where

$$\mathbf{v}_{m_k} = -\frac{\partial \mathbf{S}}{\partial m_k} \tilde{\mathbf{u}}_i \quad (8)$$

$$\mathbf{r}_i = \begin{bmatrix} \frac{1}{u_{i1}(\mathbf{m})} \log(u_{i1}(\mathbf{m})/d_{i1}) \\ \vdots \\ \frac{1}{u_{in_r}(\mathbf{m})} \log(u_{in_r}(\mathbf{m})/d_{in_r}) \\ 0 \\ \vdots \\ 0 \end{bmatrix}, \quad (9)$$

and $\tilde{\mathbf{u}}_i$ is the vector for Laplace-domain wave field from the i -th source. In Equation 7, $\mathbf{S}^{-1} \mathbf{r}_i$ is referred to the adjoint wave field or back-propagated wave field.

The gradient direction, which minimizes the misfit between the modeled and observed data, is the negative of the partial derivative of the objective function. In the conventional Laplace-domain waveform inversion, various gradient directions are normalized and summed using multiple Laplace damping constants s varying from 1 to 20 s^{-1} to correctly image the entire domain (Bae et al., 2012; Ha and Shin, 2012b; Ha et al., 2012a; Koo et al., 2011; Pyun et al., 2011; Shin et al., 2014). Finally, it is updated to the

previous velocity model using the proper step length α :

$$\mathbf{m}^{k+1} = \mathbf{m}^k - \alpha \times \mathbf{NRM} \left[\sum_{i_{damp}=1}^{n_{damp}} \mathbf{NRM} \left[\sum_{i=1}^{n_s} (\mathbf{v}_{m_k})^T \mathbf{S}^{-1} \mathbf{r}_i \right]_{i_{damp}} \right], \quad (10)$$

where k is the current iteration number, i_{damp} is the index of the damping constant, n_{damp} is total number of damping constants, and \mathbf{NRM} is a normalization operator that normalizes the contributions from each gradient using different damping constant.

The gradient direction is iteratively updated from the previous velocity model until either the data residual converges to a certain threshold ($\log(\tilde{u}) - \log(\tilde{d}) < \varepsilon$) or the current iteration number approaches the maximum iteration number ($k = k_{max}$).

2.3. Pseudo Hessian for the logarithmic objective function

To accelerate the convergence of the waveform inversion, the inverse of the Hessian matrix is multiplied by the gradient before updating the velocity model in the full-Newton and Gauss-Newton method (Pratt et al., 1998). Instead of constructing and inverting the huge Hessian matrix, Shin et al., (2001) first propose the pseudo Hessian matrix, which is a reasonable alternative to the approximated Hessian, for enhancing the image of the pre-stack reverse time migration. Using the fact that the matrix multiplication of the transposed Green's function matrix and the conjugated Green's function matrix $(\mathbf{S}^{-1})^T(\mathbf{S}^{-1})^*$ is a diagonal dominant matrix, they derive the pseudo Hessian matrix as a diagonal matrix, which considerably reduces the computing cost. More recently, Ha et al., (2012b) reformulated the pseudo Hessian matrix using the logarithmic objective function, which is generally adopted by the Laplace-domain waveform inversion, and it shows a better convergence rate than the case using the conventional pseudo Hessian matrix for the l_2 objective function. In this section of the thesis, I will introduce the pseudo Hessian for the logarithmic objective function and explain its physical meaning.

The Hessian of the logarithmic objective function can be obtained by differentiating the partial derivative logarithmic objective function (Equation 5) with respect to another l -th model parameter:

$$\begin{aligned} \frac{\partial^2 E(\mathbf{m})}{\partial m_l \partial m_k} = & \sum_{i=1}^{n_s} \sum_{j=1}^{n_r} \left[\frac{\partial^2 \tilde{u}_{ij}(\mathbf{m})}{\partial m_l \partial m_k} \left(\frac{\log(\tilde{u}_{ij}(\mathbf{m})/\tilde{d}_{ij})}{\tilde{u}_{ij}(\mathbf{m})} \right) \right. \\ & - \frac{\partial \tilde{u}_{ij}(\mathbf{m})}{\partial m_l} \frac{\partial \tilde{u}_{ij}(\mathbf{m})}{\partial m_k} \left(\frac{\log(\tilde{u}_{ij}(\mathbf{m})/\tilde{d}_{ij})}{\tilde{u}_{ij}(\mathbf{m})^2} \right) \\ & \left. + \left(\frac{1}{\tilde{u}_{ij}(\mathbf{m})} \frac{\partial \tilde{u}_{ij}(\mathbf{m})}{\partial m_l} \right) \left(\frac{1}{\tilde{u}_{ij}(\mathbf{m})} \frac{\partial \tilde{u}_{ij}(\mathbf{m})}{\partial m_k} \right) \right]. \end{aligned} \quad (11)$$

The approximated Hessian \mathbf{H}^a is obtained by ignoring the insignificant term containing the second derivative of the modeled wave field (Pratt et al., 1998):

$$\mathbf{H}_{\text{lk}}^a = \sum_{i=1}^{n_s} \sum_{j=1}^{n_r} \left[-\frac{\partial \tilde{u}_{ij}(\mathbf{m})}{\partial m_l} \frac{\partial \tilde{u}_{ij}(\mathbf{m})}{\partial m_k} \left(\frac{\log(\tilde{u}_{ij}(\mathbf{m})/\tilde{d}_{ij})}{\tilde{u}_{ij}(\mathbf{m})^2} \right) + \left(\frac{1}{\tilde{u}_{ij}(\mathbf{m})} \frac{\partial \tilde{u}_{ij}(\mathbf{m})}{\partial m_l} \right) \left(\frac{1}{\tilde{u}_{ij}(\mathbf{m})} \frac{\partial \tilde{u}_{ij}(\mathbf{m})}{\partial m_k} \right) \right], \quad (12)$$

and it can be simplified further by excluding the term containing the data residual $\log(\tilde{u}_{ij}(\mathbf{m})/\tilde{d}_{ij})$ because this term will be small enough that it can be ignored during the inversion by source estimation (Ha et al., 2012b)

$$\mathbf{H}_{\text{lk}}^a \approx \sum_{i=1}^{n_s} \sum_{j=1}^{n_r} \left[\left(\frac{1}{\tilde{u}_{ij}(\mathbf{m})} \frac{\partial \tilde{u}_{ij}(\mathbf{m})}{\partial m_l} \right) \left(\frac{1}{\tilde{u}_{ij}(\mathbf{m})} \frac{\partial \tilde{u}_{ij}(\mathbf{m})}{\partial m_k} \right) \right]. \quad (13)$$

Using the adjoint state method and a virtual source vector as in Equation 7, Equation 13 can be expressed as

$$\mathbf{H}_{\text{lk}}^a \approx \sum_{i=1}^{n_s} \left[\mathbf{v}_{m_k}^T \mathbf{S}^{-1T} \mathbf{D}_i^T \mathbf{D}_i \mathbf{S}^{-1} \mathbf{v}_{m_k} \right] \quad (14)$$

when \mathbf{D}_i is a diagonal matrix having a component of

$$\mathbf{D}_{i,j,j} = \frac{1}{\tilde{u}_{ij}(\mathbf{m})}, \quad (15)$$

and \mathbf{v}_{m_k} is a virtual source vector.

Following the approximation ($\mathbf{S}^{-1T} \mathbf{S}^{-1} = \mathbf{I}$, \mathbf{I} is an identity matrix), which was suggested by Shin et al., (2001), the pseudo Hessian for the

logarithmic objective function can be obtained as

$$\begin{aligned}
\mathbf{H}_{\text{kk}}^p &\approx \sum_{i=1}^{n_s} [\mathbf{v}_{m_k}^T \mathbf{D}_i^T \mathbf{D}_i \mathbf{v}_{m_k}] = \sum_{i=1}^{n_s} \left[\left(-\frac{\partial \mathbf{S}}{\partial m_k} \mathbf{c} \right)^T \left(-\frac{\partial \mathbf{S}}{\partial m_k} \mathbf{c} \right) \right] \\
&= n_s \left(-\frac{\partial \mathbf{S}}{\partial m_k} \mathbf{c} \right)^T \left(-\frac{\partial \mathbf{S}}{\partial m_k} \mathbf{c} \right). \tag{16}
\end{aligned}$$

$$\mathbf{c} = [1 \quad \dots \quad 1]^T$$

In Equation 16, we can see that the derived pseudo Hessian matrix is not dependent on the modeled wave field, and it is only decided by the partial derivative impedance matrix, which is proportional to s^2/m_k^3 . Therefore, the k -th diagonal component of the pseudo Hessian matrix is proportional to $1/m_k^6$ because s has a constant value in the construction of a gradient and Hessian for a single damping constant. When the gradient direction is multiplied by the inverse of the pseudo Hessian matrix, the magnitude of the gradient at an element with a velocity of m_k is scaled by m_k^6 . Thus, due to the pseudo Hessian regularization, the gradients in the high velocity areas are emphasized more than the gradients in the low velocity areas.

3. Laplace-domain waveform inversion using a single damping constant

In this section, I suggest LWI using only a single damping constant. First, single-damping LWI is performed using various damping constants that are commonly used by the conventional LWI algorithm, and the contribution of each damping constant to the inversion of the long-wavelength velocity model is identified. Second, potential issues caused by using relatively small or large damping constant in LWI are analyzed using the mathematical approach, and they are verified using numerical experiments. Subsequently, the range of proper damping constants that can be used for single-damping LWI is suggested based on the result of the numerical test. Finally, the robustness of the inversion result and the enhancement of the computing efficiency of the single-damping LWI are confirmed.

The synthetic dataset used for the numerical test is obtained from the Pluto 1.5 velocity model (Figure 1) (Stoughton et al., 2001). Even though the Pluto 1.5 velocity model was initially developed to investigate the multiple attenuation algorithms, this model is utilized as a suitable example in this study because it represents the real deep-sea environment of the Gulf of Mexico where a large number of salt domes lie. The inclined sea bottom of this model varies from 0.579 to 1.067 km, and three salt domes with different sizes and shapes are located beneath the sea floor. To avoid committing the crime that occasionally happens in studies of waveform inversion algorithms (i.e., using the same wave equation and spatial discretization method for both the observed data and the modeled data generation in the waveform inversion), the staggered grid finite difference method, which is an open source code written in Fortran 77, for the elastic wave equation is used to generate the time-domain synthetic data (Ikelle and Amundsen 2005). By setting the shear wave velocity to 0 m/s and the density to 1,000 kg/m³ for the entire area, the first-order elastic wave equation can be approximated to the acoustic wave equation using the staggered grid finite difference method. The free surface

boundary condition is applied at the top boundary, simulating interface between the seawater and air by fixing the stress component to 0. To avoid artificial reflections, which do not occur in the unbounded earth, the sponge boundary conditions is applied to the left, right, and bottom boundary by adding 50 additional nodal points as absorbing zones. To mimic the real marine survey environment, a towed streamer survey is simulated in the generation of the synthetic data. To increase the imaging aperture during the inversion, which can be restricted by the short survey distance, the velocity model is extended to the left and right, and 986 sources are used at an interval of 50 m. For the imaging area presented in Figure 1, 636 sources are included. Each source contains 1,193 receivers. The first receiver is apart from 100 m from the source, and the last receiver is 15,000 m from the source. The depth below the free surface of both sources and receivers is set to 50 m in this study. To avoid numerical instability, which can be caused by a coarse sampling interval in the explicit time domain modeling, a fine time step (0.001 s) is used, and the seismic data are recorded for 20 s. For the source wavelet, the first derivative Gaussian function with a peak frequency of 10 Hz is used (Figure 2). Figure 3 is an example of common shot gathers using the 576-th source position when the source is located at 20 km of the velocity model.

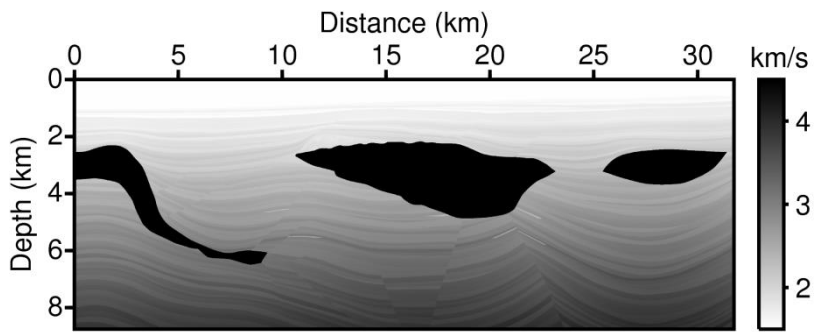


Figure 1. Pluto 1.5 velocity model

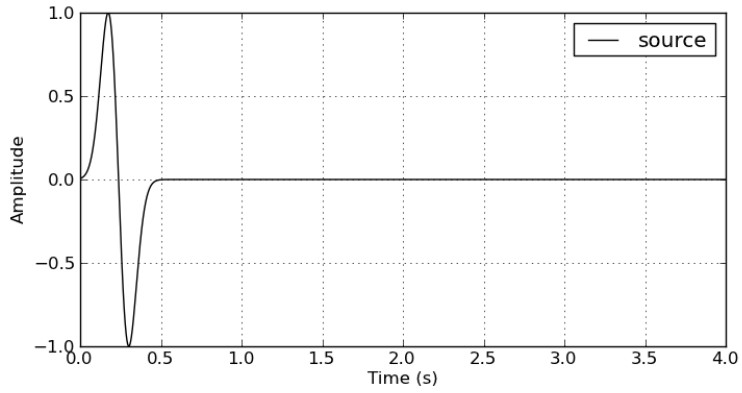


Figure 2. Source wavelet for the time domain modeling

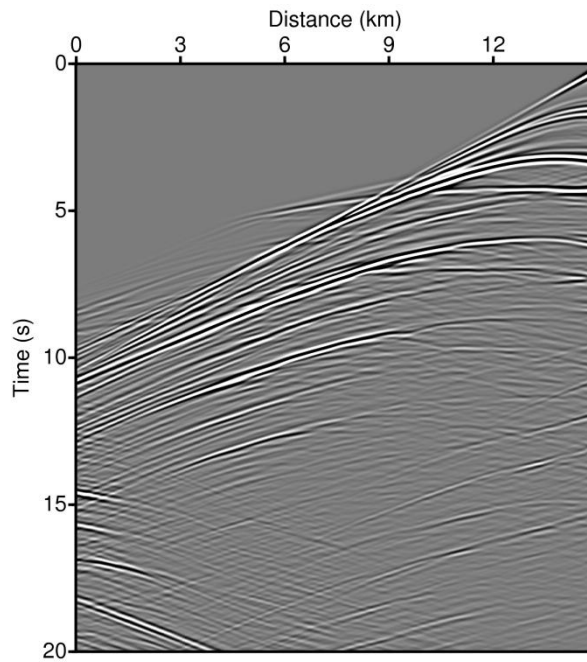


Figure 3. An example common shot gather when the source is located at 20 km of the velocity model

3.1. Resemblance of gradient direction using different damping constants

LWI shares a large portion of the algorithm with a conventional frequency domain waveform inversion (Ha et al., 2010a). The Laplace-domain wave field can be simulated using the frequency-domain wave equation and the concept of the complex angular frequency value, and the frequency-domain wave field can also be simulated using the Laplace-domain wave equation. In addition, in both waveform inversion algorithms, a group of several angular frequencies or damping constants are used either sequentially or simultaneously in the stable inversion procedures (Kim et al., 2011a; Shin et al., 2010; Sirgue and Pratt, 2004).

Despite the similarities in the computational algorithm of the frequency- and Laplace-domain waveform modeling and inversion, the wave fields in the frequency domain and in the Laplace domain have different physical meanings. The digital form of the time-domain seismic signal can be described as a summation of a number of sinusoids with unique peak amplitudes A , angular frequencies ω , and phase-lags θ , and the analysis of the time-domain signal into its sinusoidal components can be achieved via the Fourier transform (Yilmaz, 1987). In other words, using the Fourier transform (Equation 17), the time-domain signal can be broken down into various frequency-domain signals with respect to its independent frequency components, and this provides us with a good tool for analyzing the complex characteristics of a time-domain wave field.

$$\bar{u}(\omega) = \int_{-\infty}^{\infty} u(t)e^{-i\omega t} dt = Ae^{i\theta} \quad (17)$$

The Laplace transform of the time-domain seismic signal can be interpreted as the definite integration of the amplitudes of exponentially damped time domain signals:

$$\bar{u}(s) = \int_0^{\infty} v(t)dt = A, \tag{18}$$

$$v(t) = u(t)e^{-st}$$

and the results do not represent certain independent components of the original time-domain seismic signal. The different damping constants play a role only in the degree of damping before the integration. When a larger damping constant is used, the time-domain seismic signal is damped more rapidly, and a larger number of late-arrivals are lost. Figure 4 and Figure 5 show the synthetic Pluto 1.5 velocity model (the star mark indicates the source position) and its synthesized common shot gather when the receivers are located over the entire surface. When the Fourier transform is applied to the time-domain common shot gather, we can extract the independent frequency components of the original time-domain data. Figure 6 shows the normalized amplitudes of the frequency-domain wave field, and we can see that the wave field for each frequency component shows different fluctuations. Figure 7 shows the normalized amplitude of the Laplace-domain wave field on a logarithmic axis. When a large damping constant is used, the amplitude of the far offset data shows a much smaller numerical value than that of the short offset data, so a logarithmic axis is essential for displaying the Laplace-domain wave field. However, in contrast to the frequency-domain wave field, the Laplace-domain wave field for different damping constants always shows a similar smooth trend, except for the degree of damping.

The different characteristics of the wave fields in the frequency and Laplace domains are also identified in the gradient direction calculated by the waveform inversion algorithm. Figure 8a-e shows the gradient of the frequency-domain waveform inversion using the conventional l_2 objective function for various angular frequencies. The gradient using a single frequency component inverts the different wavenumber components of the background velocity model. The gradient using low frequency components inverts the long-wavelength (smooth) features of the velocity, and the gradient

using high frequency components inverts the short wavelength (detailed) features of the velocity. The wavenumber components that can be inverted using a single frequency component and the optimized selection of various frequencies are studied by many researchers (Kim et al., 2011a; Sirgue and Pratt, 2004). By summing the gradient from several frequency components, a meaningful gradient representing the true velocity model is obtained (Figure 8f).

In contrast, the gradients obtained in the Laplace domain show different characteristics than the frequency-domain gradient (Figure 9). With respect to the degree of damping, the illumination depth of the gradient shows a difference. The smaller the damping constant, the deeper the part of model imaged, and inversely, the larger the damping constant, the shallower the part of model imaged. This fact can be explained simply by two reasons. The first reason is that the damping process is applied to the time-domain seismic signals. For a smaller damping constant, a larger portion of the late arriving signals, that are reflected by the deeper part of the model survive during the integral transform, and these later arrivals are helpful in imaging the deeper part of the model. The second reason exists in the Laplace-domain wave field itself. The following equations are the analytical Green's function of the Laplace-domain wave field in 2-D and 3-D homogeneous media (Zauderer, 2006):

$$\mathbf{G}_{2-D} = \frac{1}{2\pi} K_0 \left(\frac{s}{c} |\mathbf{x} - \mathbf{x}_{src}| \right) \quad (19)$$

$$\mathbf{G}_{3-D} = \frac{e^{\left[-\frac{s}{c} |\mathbf{x} - \mathbf{x}_{src}| \right]}}{4\pi |\mathbf{x} - \mathbf{x}_{src}|} \quad (20)$$

where K_0 is a modified Bessel function, c is the speed of the compressional wave, s is the damping constant, and \mathbf{x} and \mathbf{x}_{src} are the position vectors of the receiver and source, respectively. As we can immediately confirm in

Equation 19 and 20, the Laplace-domain wave field decays exponentially with respect to the degree of the damping constant and the distance from the source. From Equation 7, we know that the Laplace-domain gradient is the dot product between the virtual source vector (which is proportional to the forward wave field) and the adjoint wave field (which is a superposition of the wave field propagated from several receivers). Because both the source and receivers are positioned on top of the velocity mode, the gradient directions in the deep areas have small absolute values, and this behavior is more severe when larger damping constants are used.

In both the frequency- and Laplace-domain waveform inversions, a group of angular frequencies or damping constants has been conventionally used because we believe that each group of frequencies (or damping constants) has different characteristics in a wave field, so it inverts the different parts of the velocity model. However, by comparing the frequency- and Laplace-domain wave fields and gradient directions, I confirm that the trends of the wave field and the gradient directions for different damping constants are not as different as those in the frequency domain. Therefore, I am motivated to reduce the computing cost of conventional LWI by minimizing the number of damping constants for the Laplace-domain waveform inversion while maintaining the accuracy of the inverted velocity model.

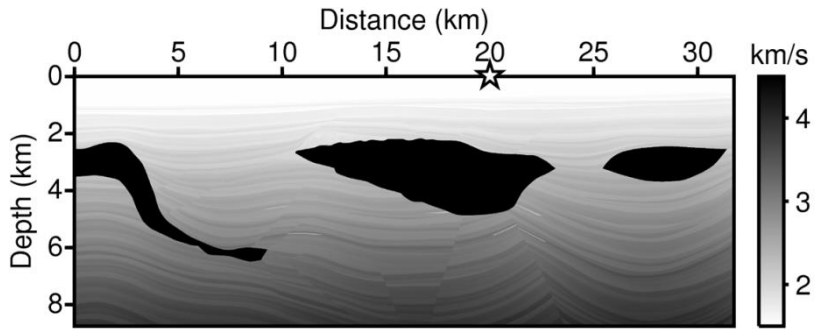


Figure 4. Pluto synthetic velocity model with a star marking the source location

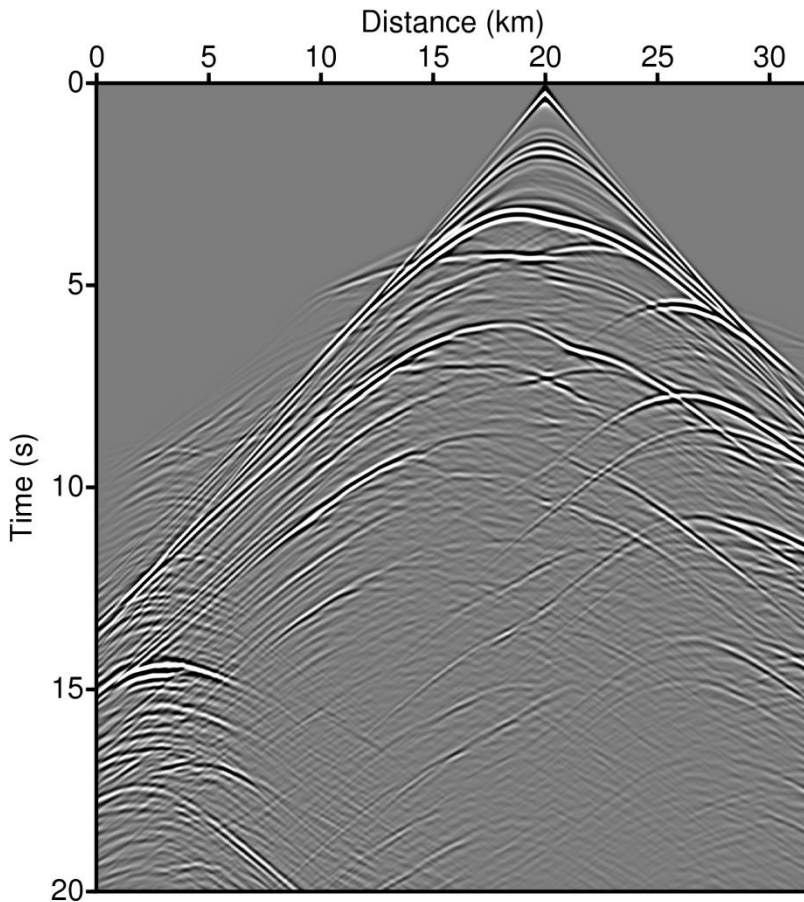


Figure 5. Synthetic common shot gather in the time domain when the source is located at the star in Figure 4 and receivers are located over at the entire surface

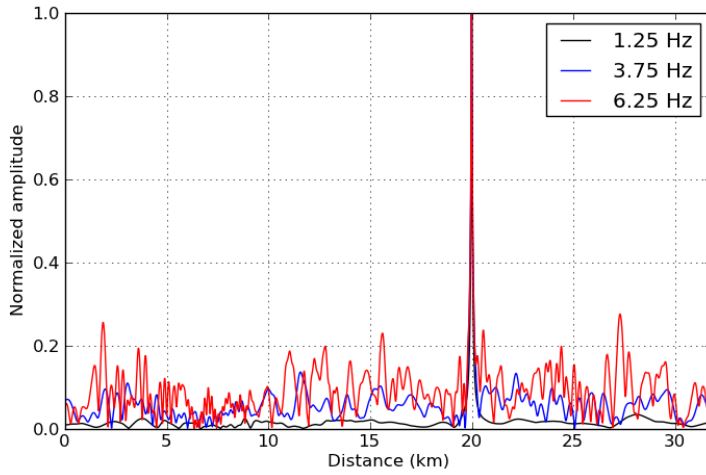


Figure 6. Synthetic common shot gathers in the frequency domain for three discrete frequencies (1.25, 3.75, and 6.25 Hz)

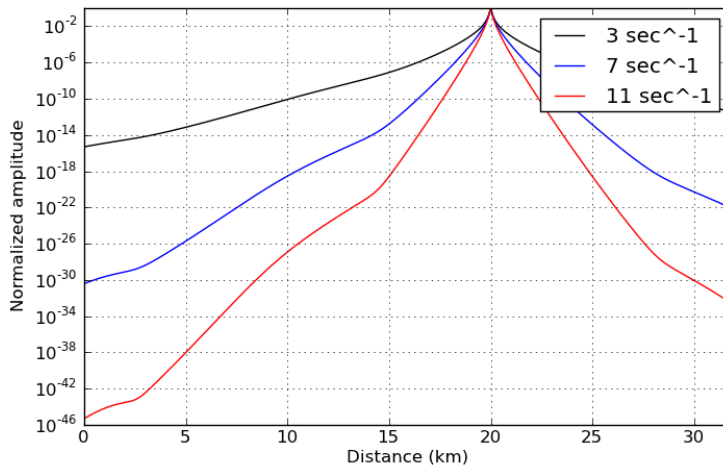


Figure 7. Synthetic common shot gathers in the Laplace domain for three damping constants (3, 7, and 11 s^{-1})

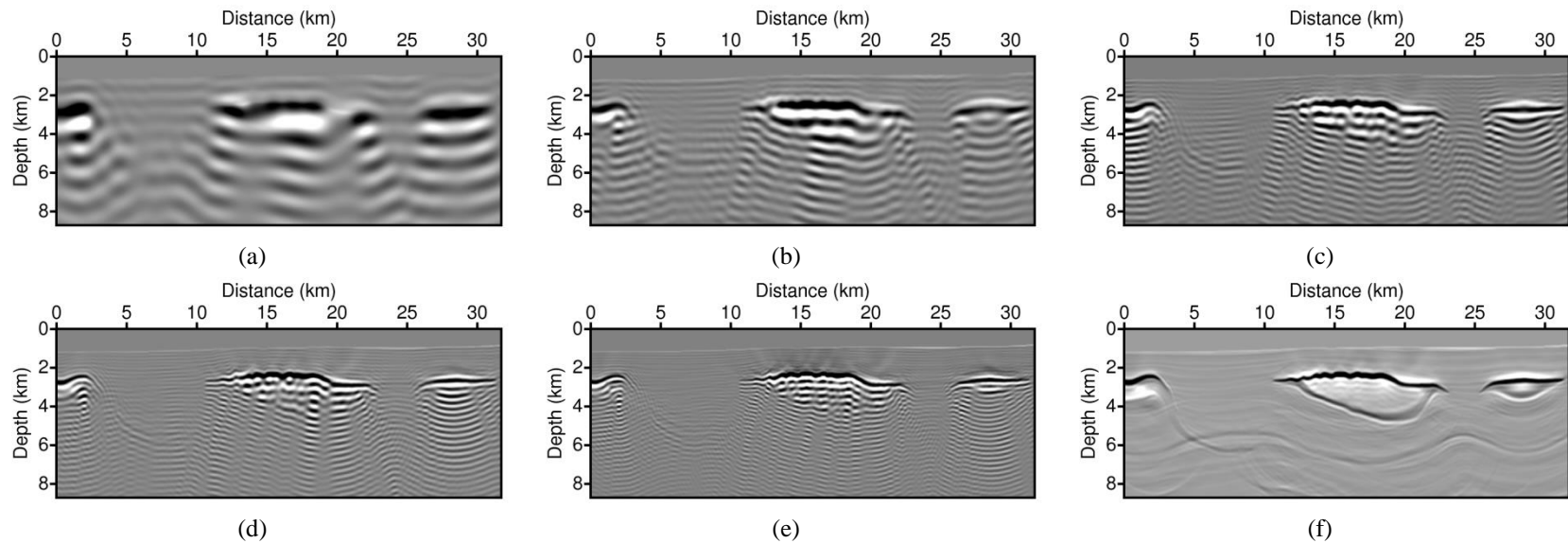


Figure 8. Frequency-domain gradient direction using (a) 1.25, (b) 2.5, (c) 3.75, (d) 5, and (e) 6.25 Hz. (f) is a summed gradient using 24 frequencies between 1.25 and 7 Hz at an interval of 0.25 Hz

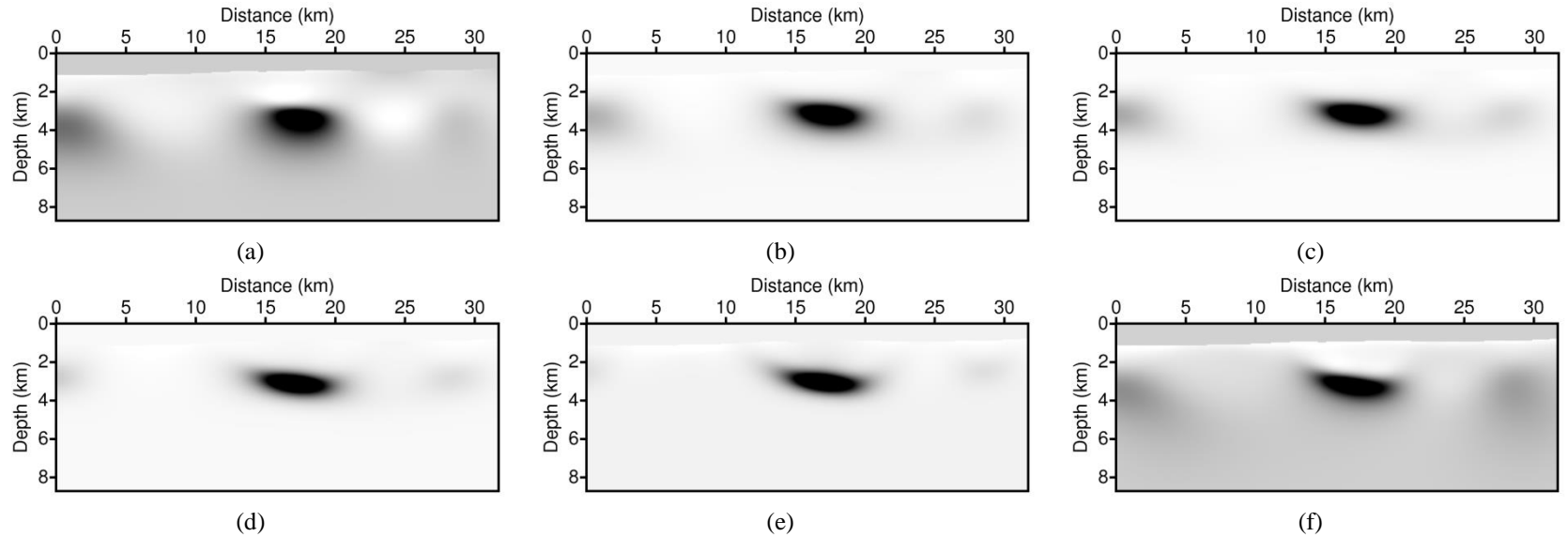


Figure 9. Laplace-domain gradient using (a) 3, (b) 5, (c) 7, (d) 9, and (e) 11 s^{-1} . (f) is a summed gradient using 7 damping constants between 1 and 13 s^{-1} at an interval of 2 s^{-1}

3.2. Inversion results for different damping constants

In this section, the single-damping LWI is performed using various damping constants ($1\sim 15\text{ s}^{-1}$), which are typical candidates used by the conventional LWI to identify the contribution of each damping constant in the inversion of the long-wavelength velocity model. The two-layered homogeneous velocity model with a water layer is used as an initial velocity model (Figure 10). For the stopping criterion, the maximum number of iteration is defined as 200 with the fixed step length of 50 m/s. During the inversion, the velocity at the water layer is fixed at 1,500 m/s without updating the gradient directions, and the updated velocity model is constrained between 1,500 and 4,514 m/s.

Figure 11 shows the inverted velocity model obtained by the single-damping LWI using 15 different damping constants ranging from 1 to 15 s^{-1} . Small damping constants invert the macro area covering the deep part as well as the shallow part of the model because the Laplace-transformed data using a smaller damping constant contain more late-arrivals, which are reflected by the deeper part of the model, compared to those using large damping constants, and numerical wave fields with small damping constants are able to propagate into the deeper part of the model. However, small damping constants (e.g., 1, 2, and 3 s^{-1}) do not provide us with the proper resolution, so the inverted velocity model shows blurred image without performing the enough velocity updates at the shallow part of the model. For the case using the smallest damping constant of 1 s^{-1} , the inverted high-velocity areas are located in the wrong positions vertically compared to the true velocity model. In contrast, large damping constants properly update the shallow part of the model, which provides us with more detailed results. However, the imaging depth is too restricted, especially when the damping constant is larger than or equal to 10 s^{-1} , which is explained by the decaying property of Laplace-domain wave propagation and the lost far-offset data during the Laplace transform for large damping constants (this will be explained in section of 3.3). Meanwhile, the inverted velocity model with a medium damping

constant, such as 4, 5, 6, 7, 8, or 9 s⁻¹, follows the correct trend for the long-wavelength components of the true velocity model.

For more detailed quantitative analysis, we compute the relative model misfit $\xi(\mathbf{m}_{\text{cal}})$ for the inverted velocity model using the following equation, which is adopted from Prioux et al. (2013);

$$\xi(\mathbf{m}_{\text{cal}}) = \frac{100}{N_x N_z} \sum_{i=1}^{N_x N_z} \frac{|m_{\text{cal},i} - m_{\text{true},i}|}{m_{\text{true},i}}, \quad (21)$$

where N_x and N_z are the number of elements in the x and z directions in the Cartesian grid, and $m_{\text{cal},i}$ and $m_{\text{true},i}$ are the inverted and true velocity components of the i -th element. Figure 12 shows the relative model misfit of the Laplace-domain inverted velocity model for 15 different damping constants ranging from 1 to 15 s⁻¹. As expected from the images from the inverted velocity models, the small damping constants between 1 and 3 s⁻¹ and the large damping constants between 10 and 15 s⁻¹ show large difference from the true velocity model, indicating that they do not represent the entire long-wavelength velocity model. The inverted velocity model using a damping constant of 5 s⁻¹ shows the smallest deviation from the true velocity model, and the damping constants ranging from 4 to 9 s⁻¹ show only a 0.5 % difference from the optimal damping constant of 5 s⁻¹.

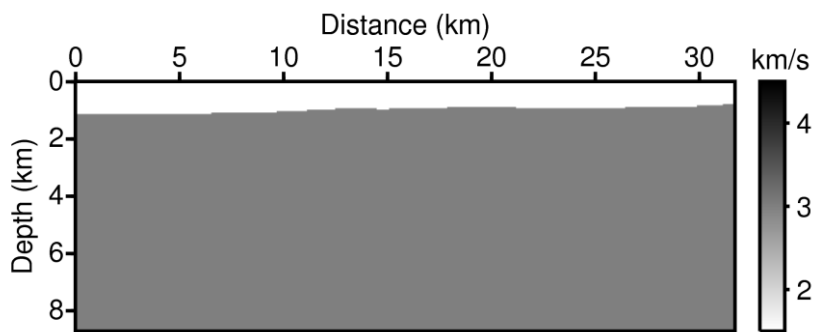


Figure 10. The two-layered homogeneous velocity model for LWI

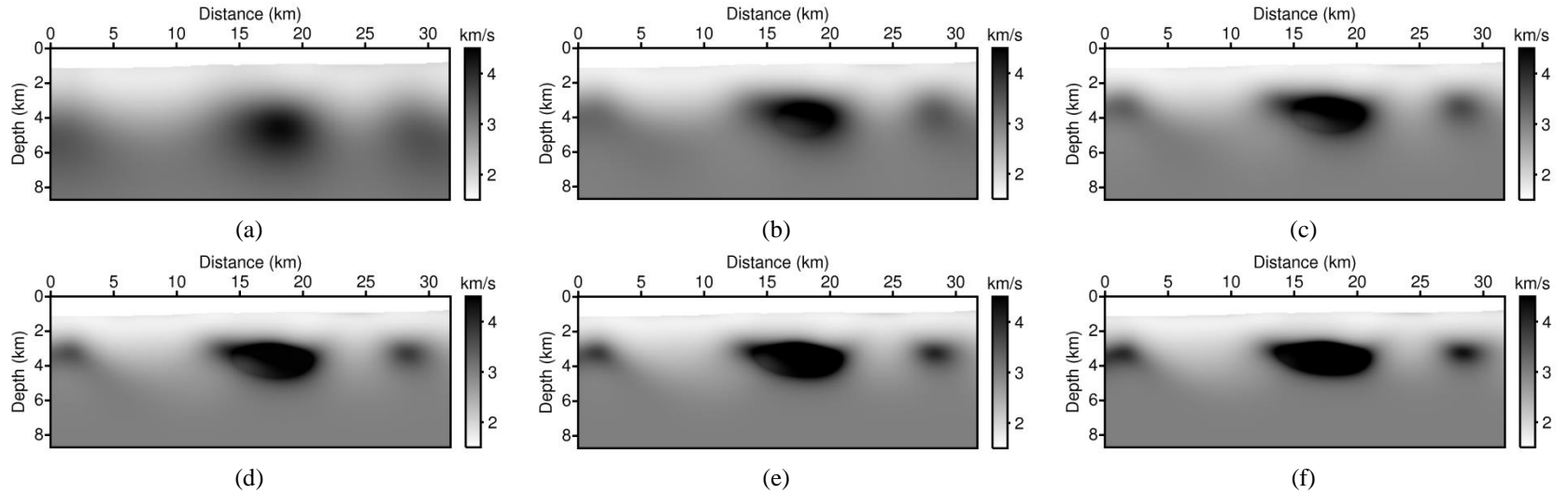
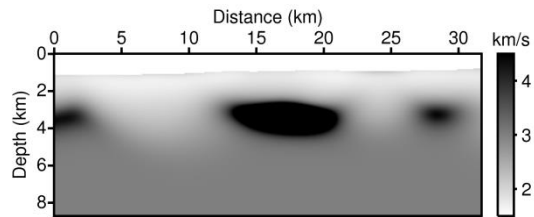
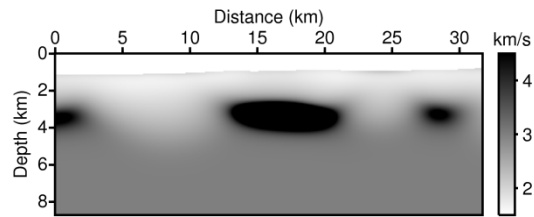


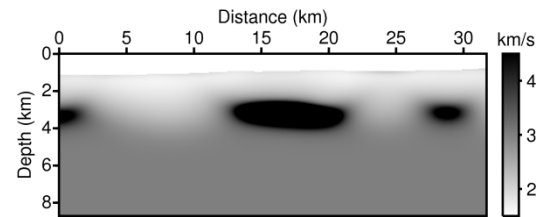
Figure 11. Inverted velocity model obtained by single-damping LWI using a damping constant of (a) 1, (b) 2, (c) 3, (d) 4, (e) 5, (f) 6, (g) 7, (h) 8, (i) 9, (j) 10, (k) 11, (l) 12, (m) 13, (n) 14, and (o) 15 s^{-1}



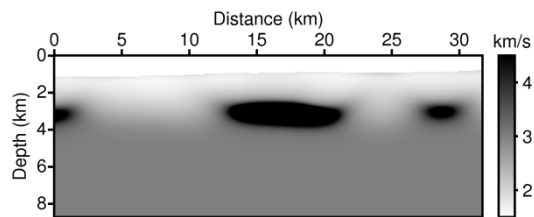
(g)



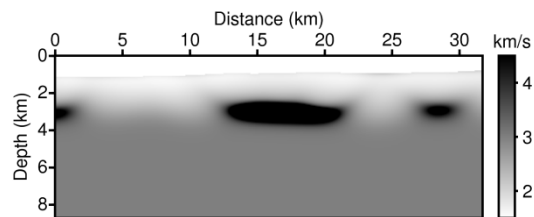
(h)



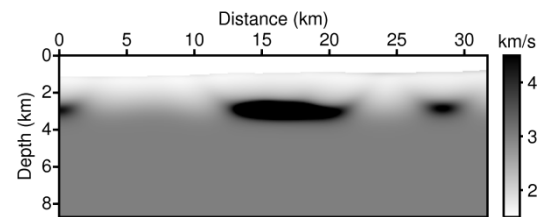
(i)



(j)

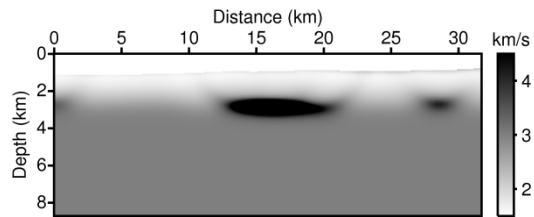


(k)

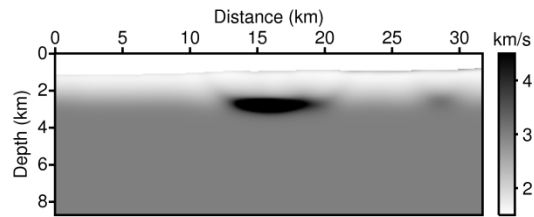


(l)

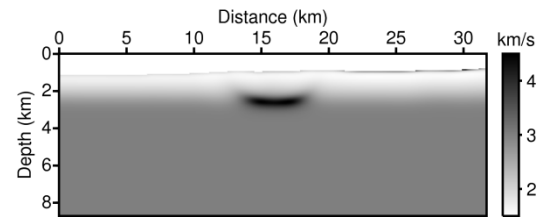
(Continued)



(m)



(n)
(Continued)



(o)

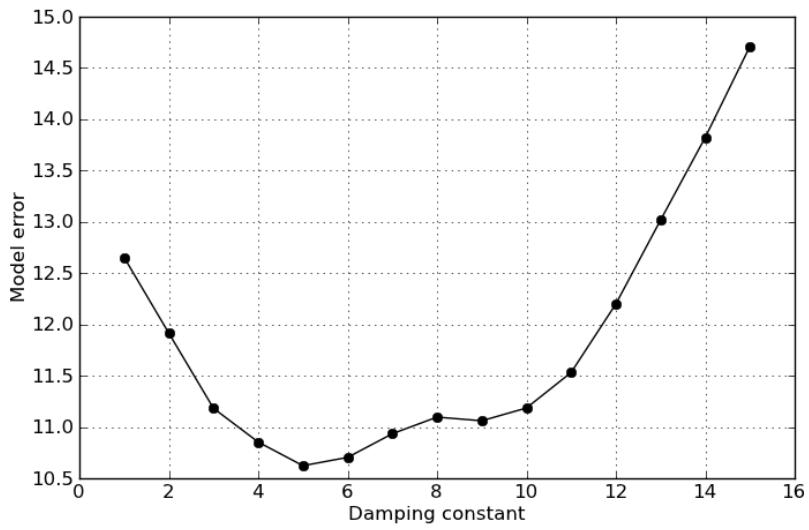


Figure 12. Relative model misfit of the Laplace-domain inverted velocity model for different damping constants

3.3. Issues in the gradient direction using small and large damping constants

3.3.1. Imperfect Laplace transform due to the finite listening time

During seismic acquisition, the seismic data are originally acquired as digital time-domain data. When we apply the LWI algorithm to those data to construct the long-wavelength (smooth) velocity model, the observed data should be obtained through the Laplace transform of the time domain seismic data. Theoretically, the exact Laplace transform of the time domain signal should be performed via definite integration from zero to positive infinite time (Equation 1). However, in real marine seismic exploration, the acquisition of data with infinite (or very long) listening times cannot be realized. In marine seismic exploration, the boat towing the source and receiver streamers needs to travel at a certain speed (e.g., 8 km/h) to control the streamer equipment, properly. In addition, the shot spacing needs to be small enough (e.g., 25~50 m) to increase the common midpoint fold to enhance the resolution for various seismic signal processing applications. Therefore, the maximum listening time is restricted by the relationship between the shot spacing and the speed of the boat. For instance, the typical listening time for marine seismic exploration would be less than 10 s. Therefore, the theoretically ideal Laplace transform of seismic data with finite listening time should be approximated by damping out the late-arrivals in the time trace using sufficiently large damping constants. Inversely, small damping constants can cause an inaccurate Laplace transform of the seismic data.

To investigate how much the length of listening time affects the results of the LWI, the logarithmic residuals of the modeled and observed wave fields ($\log \tilde{u} - \log \tilde{d}$ term in Equation 5) are compared with respect to different listening times and damping constants. For the simple mathematical investigation, the ideal observed wave field $d_{\infty}(t)$ (Figure 13a) with an infinite listening time is assumed to be a causal sinusoid (this assumption can be established because any time signal can be thought of as superposition of

various causal sinusoids) as follows:

$$d_{\infty}(t) = A \sin \omega(t - T_f)H(t - T_f), \quad (22)$$

where A is the maximum amplitude, ω is the angular frequency, T_f is the recorded time for the first break, and H is the Heaviside step function.

In the same manner, the observed wave field $d_{T_{max}}$ (Figure 13b) with a finite listening time T_{max} can be expressed as follows:

$$d_{T_{max}}(t) = A \sin \omega(t - T_f)\{H(t - T_f) - H(t - T_{max})\}. \quad (23)$$

Then, the difference between $d_{\infty}(t)$ and $d_{T_{max}}(t)$ can be obtained

$$d_{error}(t) = d_{\infty}(t) - d_{T_{max}}(t) = A \sin \omega(t - T_f)H(t - T_{max}), \quad (24)$$

and using the properties of trigonometric functions, it can be rewritten as

$$d_{error}(t) = A\{\sin \omega(t - T_{max}) \cos \omega(T_{max} - T_f) + \cos \omega(t - T_{max}) \sin \omega(T_{max} - T_f)\}H(t - T_{max}). \quad (25)$$

The shifted function $f(t - a)$, which is multiplied with the Heaviside step function $H(t - a)$ can be transformed into the Laplace domain as follows (\mathcal{L}_s is the Laplace transform operator for the damping constant s):

$$\mathcal{L}_s\{f(t - a)H(t - a)\} = e^{-as}\tilde{f}(s), \quad (26)$$

thus, Equation 22 and 25 can be analytically transformed into the Laplace domain as

$$\tilde{d}_\infty(s) = Ae^{-sT_f} \frac{\omega}{s^2 + \omega^2}, \quad (27)$$

and

$$\begin{aligned} \tilde{d}_{error}(s) = Ae^{-sT_{max}} \left\{ \frac{\omega}{s^2 + \omega^2} \cos \omega(T_{max} - T_f) \right. \\ \left. + \frac{s}{s^2 + \omega^2} \sin \omega(T_{max} - T_f) \right\} \end{aligned} \quad (28)$$

when $\tilde{d}_\infty(s)$ and $\tilde{d}_{error}(s)$ is Laplace-transformed $d_\infty(t)$ and $d_{error}(t)$, respectively, using a damping constant of s .

Finally, the Laplace-transformed wave field $\tilde{d}_{T_{max}}(s)$ with a finite listening time for a damping constant of s can be obtained by subtracting Equations 27 and 28 because $\tilde{d}_{T_{max}}$ equals $\tilde{d}_\infty - \tilde{d}_{error}$ using the linear property of the Laplace transform, and it is

$$\begin{aligned} \tilde{d}_{T_{max}}(s) = A \left[e^{-sT_f} \frac{\omega}{s^2 + \omega^2} \right. \\ \left. - e^{-sT_{max}} \left\{ \frac{\omega}{s^2 + \omega^2} \cos \omega(T_{max} - T_f) \right. \right. \\ \left. \left. + \frac{s}{s^2 + \omega^2} \sin \omega(T_{max} - T_f) \right\} \right]. \end{aligned} \quad (29)$$

Then, the logarithmic residual ($\log \tilde{u} - \log \tilde{d}$ or $\log \frac{\tilde{u}}{\tilde{d}}$), which is minimized during the Laplace-domain waveform inversions, between $\tilde{u}(s)$ and $\tilde{d}_{T_{max}}(s)$ and between $\tilde{u}(s)$ and $\tilde{d}_\infty(s)$, satisfy the following relations:

$$\log \left(\frac{\tilde{u}(s)}{\tilde{d}_{T_{max}}(s)} \right) = \log \left(\frac{\tilde{u}(s)}{\tilde{d}_\infty(s)} \right) - \varepsilon \quad (30)$$

when

$$\mathcal{E} = \log\left(\frac{\tilde{d}_{T_{max}}(s)}{\tilde{d}_{\infty}(s)}\right). \quad (31)$$

In the above relations (Equation 30), \mathcal{E} indicates the difference between two logarithmic residuals $\log\left(\frac{\tilde{u}(s)}{\tilde{d}_{T_{max}}(s)}\right)$ and $\log\left(\frac{\tilde{u}(s)}{\tilde{d}_{\infty}(s)}\right)$ caused by the imperfect Laplace transform due to the finite listening time. By inserting Equations 27 and 29 into Equation 31, \mathcal{E} can be calculated as

$$\mathcal{E} = \log(1 - \mathcal{F}) \quad (32)$$

where the function \mathcal{F} is

$$\begin{aligned} \mathcal{F} &= e^{-s(T_{max}-T_f)} \left\{ \cos \omega(T_{max} - T_f) + \frac{s}{\omega} \sin \omega(T_{max} - T_f) \right\} \\ &= e^{-s(T_{max}-T_f)} \sqrt{1 + \frac{s^2}{\omega^2}} \sin(\omega(T_{max} - T_f) + \alpha) \\ &= \mathcal{L}[s; T_{max} - T_f] \mathcal{M}[s; \omega] \mathcal{H}[s; \omega; T_{max} - T_f] \end{aligned} \quad (33)$$

$$\begin{aligned} \mathcal{L} &= e^{-s(T_{max}-T_f)} \\ \mathcal{M} &= \sqrt{1 + \frac{s^2}{\omega^2}} \\ \mathcal{H} &= \sin(\omega(T_{max} - T_f) + \alpha) \\ \alpha &= \frac{s}{\omega} / \sqrt{1 + \frac{s^2}{\omega^2}} \end{aligned}$$

The absolute value of \mathcal{F} needs to be small enough to minimize the difference, \mathcal{E} , between logarithmic residuals using the observed data with finite and infinite listening times. In Equation 33, the function \mathcal{H} is an oscillatory sinusoidal function that varies arbitrarily from -1 to 1 and is largely dependent on ω and $T_{max} - T_f$ rather than s . Therefore, we can define the maximum absolute value of \mathcal{F} by setting \mathcal{H} as 1 as follows:

$$|\mathcal{F}|_{max} = \mathcal{L}[s; T_{max} - T_f] \mathcal{M}[s; \omega].$$

$$\mathcal{L} = e^{-s(T_{max}-T_f)} \quad (34)$$

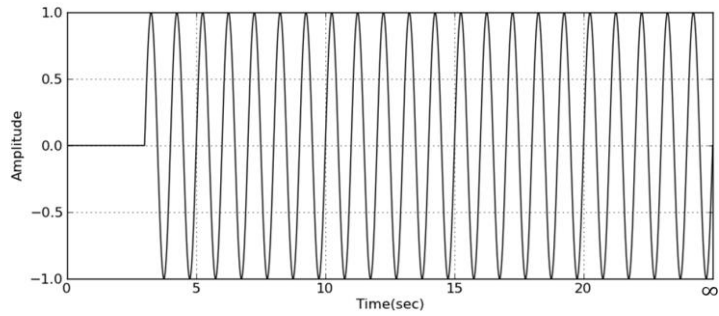
$$\mathcal{M} = \sqrt{1 + \frac{s^2}{\omega^2}}$$

Equation 34 is a function of the damping constant s , angular frequency ω , and the listening time of the seismic signal after the first break $T_{max} - T_f$. $T_{max} - T_f$ is an argument of the function \mathcal{L} , and it indicates that a long listening time is helpful for minimizing $|\mathcal{F}|_{max}$. ω is an argument of the function \mathcal{M} , and it indicates that a large angular frequency is helpful for minimizing $|\mathcal{F}|_{max}$. In contrast to $T_{max} - T_f$ and ω , s is an argument for both \mathcal{L} and \mathcal{M} . However, \mathcal{L} decays much faster than \mathcal{M} , which grows as a larger damping constant s is used. This result indicates that the logarithmic residual $\log\left(\frac{\tilde{u}(s)}{\tilde{d}_{T_{max}}(s)}\right)$ can be successfully approximated to $\log\left(\frac{\tilde{u}(s)}{\tilde{d}_{\infty}(s)}\right)$ by using a large damping constant s . In contrast, if the damping constant s is small, $|\mathcal{F}|_{max}$ is not small enough to minimize the difference \mathcal{E} . In this situation, artificial residuals can be detected even when using the true velocity model as the initial velocity model for inversion, which leads to the wrong final solution of the waveform inversion.

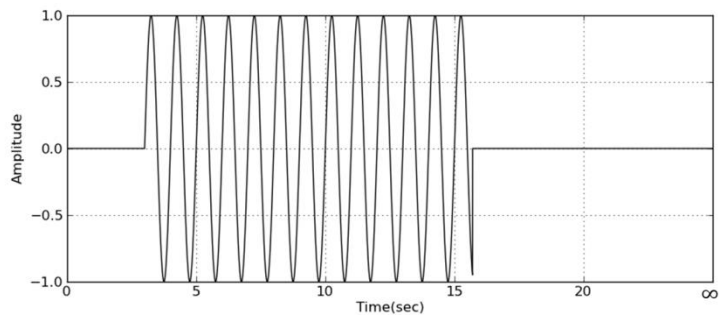
Subsequently, I carry out a numerical experiment to investigate the effects caused by the finite listening time on the inverted velocity model. The Laplace-domain inverted velocity model shown in the previous section 3.2 is obtained by inverting the observed data having a maximum listening time of 20 s, and the Laplace transform of these data is successfully approximated to the theoretically ideal Laplace transform for all damping constants ($1\sim 15 \text{ s}^{-1}$). However, it requires an unrealistically long listening time, which cannot be realized in conventional towed-streamer marine surveys. Here, I investigate what happens to the Laplace-domain inverted velocity model when the maximum listening time is reduced to 16, 12, and 8 s to mimic more realistic seismic acquisition (Figure 14) without modifying any of the modeling and

inversion algorithms.

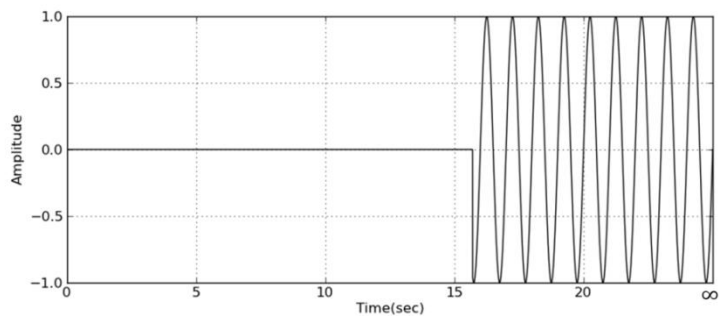
Figure 15 is the inverted velocity model obtained by the single-damping LWI using relatively small damping constants ranging from 1 to 6 s^{-1} for data with a maximum listening time of 16 s. When the maximum listening time is 16 s, the results of single-damping LWI do not make a significant difference compared with the case using 20 s-listening time data. When the listening time is longer than 16 s, the damping constants, which are larger than or equal to 1 s^{-1} , are able to produce stable results by approximating the ideal Laplace transformation using finite-listening time data. Figure 16 is the inverted velocity model for 12 s-listening time data. For data with a shorter listening time, the inverted velocity model using the smallest damping constant of 1 s^{-1} distorts the inversion result severely, but damping constants larger than or equal to 2 s^{-1} still produce robust inversion results. Similarly, Figure 17 shows the same comparison for 8 s-listening time data, and damping constants of 2 and 3 s^{-1} also produce severe artifacts as does the case of the damping constant of 1 s^{-1} due to the inversion of high velocity artifacts from the deep part of the model that do not exist in the true velocity model. An inverted velocity model using a damping constant of 4 s^{-1} also shows a slight difference from the inverted model when using datasets with longer listening times. A large amount of the real data acquired from towed-streamer surveys have listening times as short as 8 s. Therefore, for the inversion of these data with short listening times, it is better to exclude damping constants that are as small as 4 s^{-1} to prevent distortion of the velocity model.



(a)



(b)



(c)

Figure 13. Causal sinusoids having (a) infinite listening time and (b) finite listening time, and (c) the difference between (a) and (b). In these figures, A is 1, ω is 2π , T_{max} is 15.7, and T_f is 3.0.

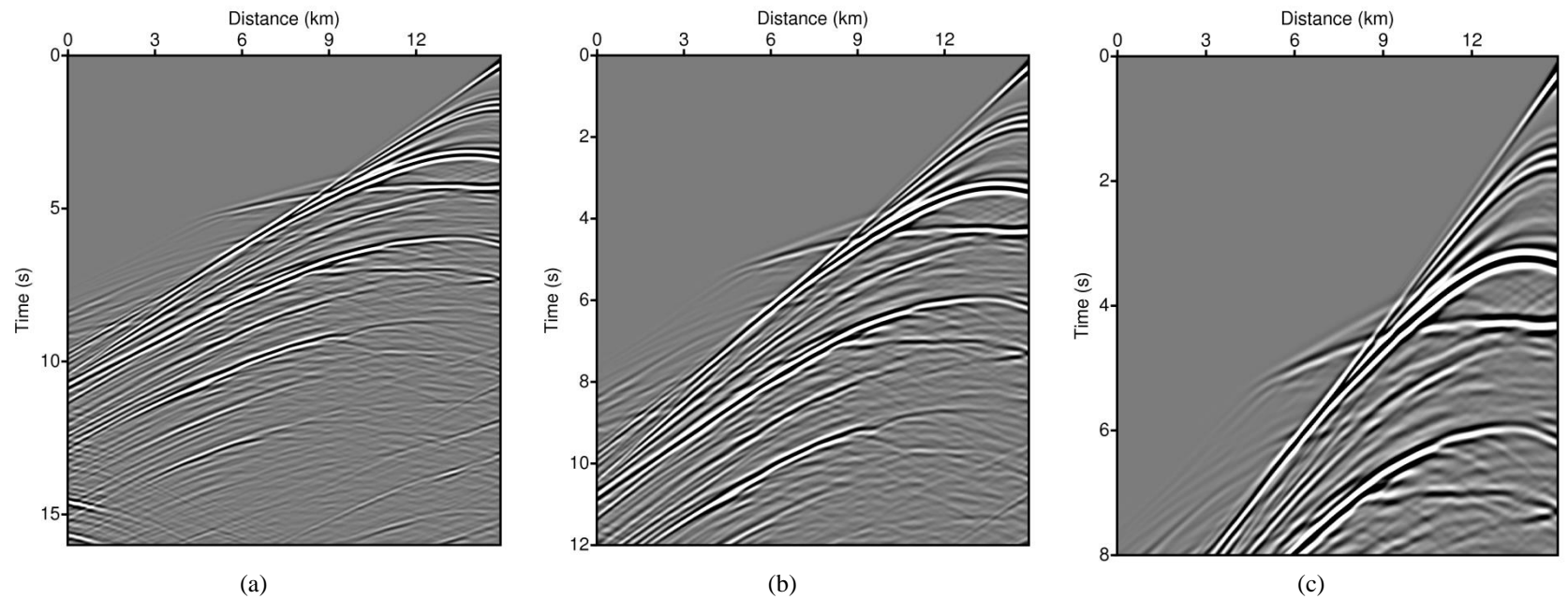


Figure 14. Example common shot gathers with maximum listening times of (a) 16, (b) 12, and (c) 8 s when the source is located at 20 km of the velocity model

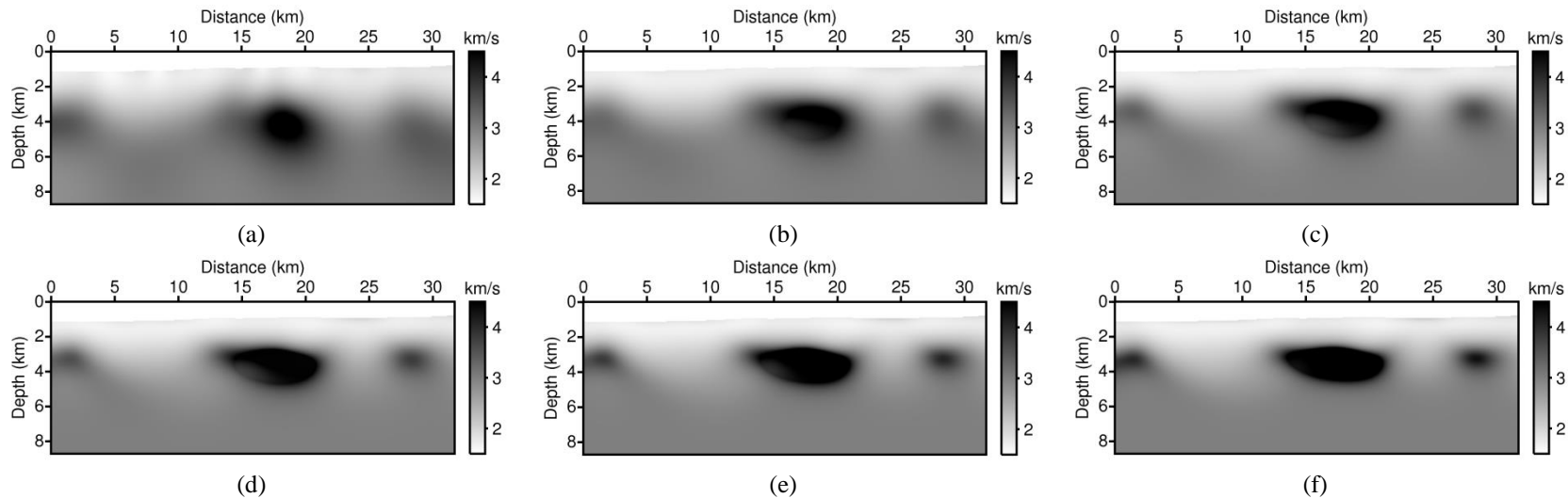


Figure 15. Inverted velocity model obtained by single-damping LWI using a damping constant of (a) 1, (b) 2, (c) 3, (d) 4, (e) 5, and (f) 6 s⁻¹ for synthetic data with a maximum listening time of 16 s

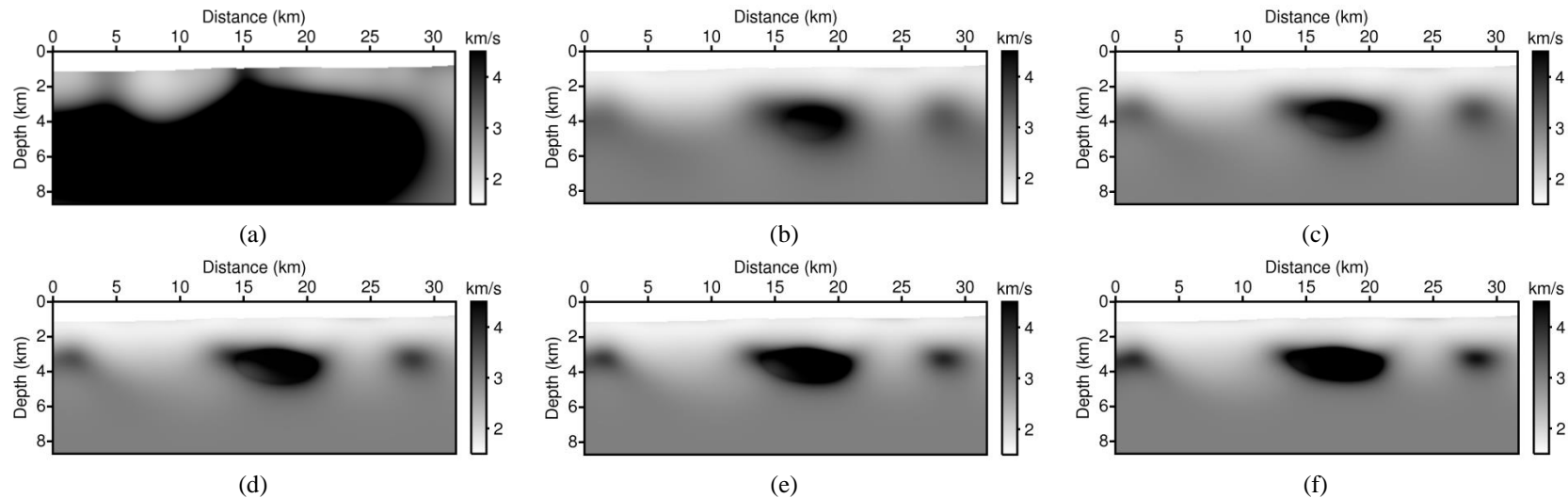


Figure 16. Inverted velocity model obtained by single-damping LWI using a damping constant of (a) 1, (b) 2, (c) 3, (d) 4, (e) 5, and (f) 6 s^{-1} for synthetic data with a maximum listening time of 12 s

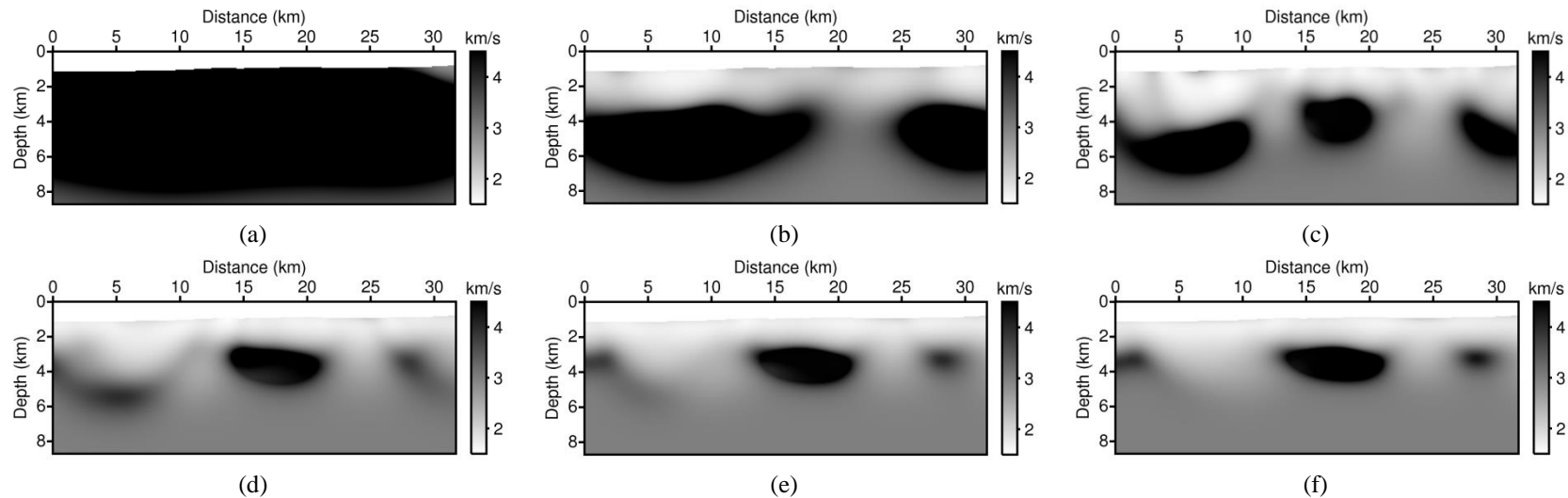


Figure 17. Inverted velocity model obtained by single-damping LWI using a damping constant of (a) 1, (b) 2, (c) 3, (d) 4, (e) 5, and (f) 6 s^{-1} for synthetic data with a maximum listening time of 8 s

3.3.2. Sensitivity to noise

The seismic data acquired in real marine environments can be contaminated by noise from various sources, and there have been several studies to reduce the effects of noise in successful waveform inversion by selecting the proper objective functions (Amunsen, 1991; Crase et al., 1990; Guitton and Symes, 2003; Ha et al., 2009). When we apply the Laplace transform to time domain data contaminated by several noises, the degree of the side effects caused by the noises can be decided by the damping constant. To investigate the influence of noise on LWI, the logarithmic residuals of the noise-free and noise-contaminated wave field are compared mathematically. For the simple analysis, I assume that a trace of the time-domain modeled wave field $u(t)$ is the time-shifted modeled seismic signal $f_u(t - T_u)$ as much as the time for the first-break T_u :

$$u(t) = f_u(t - T_u)H(t - T_u). \quad (35)$$

In the same manner, the noise-free observed wave field $d_{ideal}(t)$, pure noise $n(t)$, and noise-contaminated observed wave field $d_{noisy}(t)$ can be expressed as follows:

$$d_{ideal}(t) = f_d(t - T_d)H(t - T_d) \quad (36)$$

$$n(t) = f_n(t - T_n)H(t - T_n) \quad (37)$$

$$d_{noisy}(t) = f_d(t - T_d)H(t - T_d) + f_n(t - T_n)H(t - T_n), \quad (38)$$

where $f_d(t - T_d)$ and $f_n(t - T_n)$ are the time-shifted observed signal and the pure noise signal, respectively, T_d and T_n are their travel times, and H is the Heaviside step function. Because any noise before the first arrival is artificially muted before performing the Laplace transform in the real data application of the LWI algorithm, T_n is always assumed to be larger than or

at least equal to T_d .

The Laplace transformed Equations 35, 36 and 38 can be written as

$$\tilde{u}(s) = \tilde{f}_u(s)e^{-sT_u} \quad (39)$$

$$\tilde{d}_{ideal}(s) = \tilde{f}_d(s)e^{-sT_d} \quad (40)$$

$$\tilde{d}_{noisy}(s) = \tilde{f}_d(s)e^{-sT_d} + \tilde{f}_n(s)e^{-sT_n} \quad (41)$$

when $\tilde{u}(s)$, $\tilde{d}_{ideal}(s)$, $\tilde{d}_{noisy}(s)$, $\tilde{f}_u(s)$, $\tilde{f}_d(s)$, and $\tilde{f}_n(s)$ represent Laplace-transformed $u(t)$, $d_{ideal}(t)$, $d_{noisy}(t)$, $f_u(t)$, $f_d(t)$, and $f_n(t)$.

Then, logarithmic residual ($\log \tilde{u} - \log \tilde{d}$ or $\log \frac{\tilde{u}}{\tilde{d}}$) between $\tilde{u}(s)$ and $\tilde{d}_{ideal}(s)$, and the one between $\tilde{u}(s)$ and $\tilde{d}_{noisy}(s)$ have the following relations

$$\log\left(\frac{\tilde{u}(s)}{\tilde{d}_{ideal}(s)}\right) = \log\left(\frac{\tilde{u}(s)}{\tilde{d}_{noisy}(s)}\right) + \mathcal{E} \quad (42)$$

when

$$\mathcal{E} = \log\left(\frac{\tilde{d}_{noisy}(s)}{\tilde{d}_{ideal}(s)}\right). \quad (43)$$

In the above relations (Equations 42 and 43), \mathcal{E} indicates the difference between the two residuals $\log\left(\frac{\tilde{u}(s)}{\tilde{d}_{ideal}(s)}\right)$ and $\log\left(\frac{\tilde{u}(s)}{\tilde{d}_{noisy}(s)}\right)$ caused by the noise recorded after the first arrival. By inserting Equations 40 and 41 into Equation 43, \mathcal{E} can be calculated as

$$\mathcal{E} = \log(1 + \mathcal{F}) \quad (44)$$

where \mathcal{F} is

$$\mathcal{F} = \frac{\tilde{f}_n(s)}{\tilde{f}_d(s)} e^{-s(T_n - T_d)} \quad (45)$$

The absolute value of \mathcal{F} needs to be small enough to minimize the difference, \mathcal{E} , between the logarithmic residuals using the observed data from the noise-free and noise-contaminated environments. Equation 45 is a function of three arguments $\frac{\tilde{f}_n(s)}{\tilde{f}_d(s)}$, $T_n - T_d$, and s . The first argument is thought of as an inverse of the signal-to-noise ratio in the Laplace domain, and it is straightforward that the large signal-to-noise ratio (or small $\frac{\tilde{f}_n(s)}{\tilde{f}_d(s)}$) is helpful for minimizing function \mathcal{F} . The second argument is the difference in the arrival time between the noise signal and the observed signal, and the later the noise signal arrived, the smaller value of \mathcal{F} . This also indicates that the noise-mute process in the Laplace-domain waveform inversion is very important to minimize the effect caused by the noise. The final argument is the s for the Laplace transform. Because the negative value of s is an argument of the exponential function, a larger s minimizes \mathcal{F} , and the difference between the two residual are neglected successfully.

Subsequently, I carry out a numerical experiment to investigate the effects caused by the noise. For various seismic processing algorithms for imaging the subsurface, all types of unwanted signals are regarded as noises. Among them, random noises refer to the unwanted signals that do not have consistent phases and amplitudes. Most random noises do not originate from subsurface structures, but they can be generated by various factors, such as wave motion in marine surveys, traffic and wind in land surveys, and by the electronic devices that are used for the seismic acquisition. For the experiment, the random noises are artificially generated and added to the noise-free

synthesized data using open source seismic processing software (Seismic Unix). Random noises are originally distributed for all traces and entire time intervals. However, the random noises arriving before the first arrival have a negative influence on the Laplace transform of the time domain data, so the random noises before the first arrival are artificially muted. An example of noise-contaminated data is shown in Figure 19. Figure 20 is a comparison of an example trace with and without random noise.

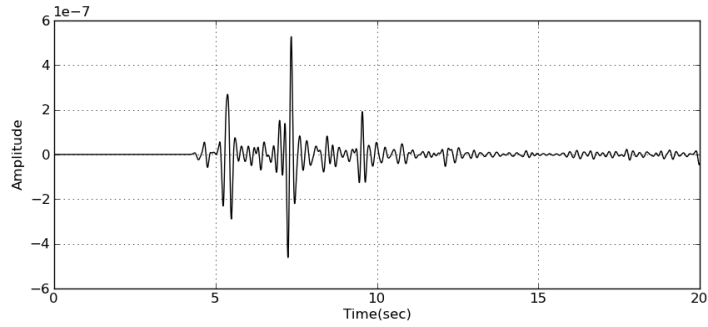
Single-damping LWI is performed using 6 relatively small damping constants ranging from 1 to 6 s⁻¹ for data contaminated by random noises. The various settings (e.g., initial velocity model, velocity constraint, stopping criterion, and step length) for the inversion are the same as in the examples in section 3.2. The inverted velocity model using a damping constant of 1 s⁻¹ is extremely overestimated for the entire area (Figure 21a). Most parts of the model are updated to the maximum constraint of the velocity update. The results for the rest of the damping constants also deviate from the inverted velocity model with noise-free data, but the degree of the distortion of the inverted velocity model is different for different damping constants (Figure 21b-f). To explain this result, we need to remember Equation 45. When the random noises that arrived before the first arrival are artificially muted, T_n is equal to T_d , and the exponential term in Equation 45 has the same value of 1 irrespective of the damping constant s . The damping constant decides only the term of $\frac{\tilde{f}_n(s)}{\tilde{f}_d(s)}$ indicating the inverse of the signal-to-noise ratio in the Laplace domain, but this value is never approximated as zero by managing the damping constant for the Laplace transform. This is the reason that the artifacts are found in all inversion results (Figure 21). In Figure 20, we can see that the amplitude of the seismic signal is small for the late arrivals compared to the early arrivals due to the attenuation property of wave propagation. However, the random noises have similar amplitudes for all of the time intervals. Therefore, the term $\frac{\tilde{f}_n(s)}{\tilde{f}_d(s)}$ has a smaller value (but not approximated as zero) for large damping constants, so the level of distortion is determined

by the damping constants, and larger damping constants provide us results which are less affected by noises.

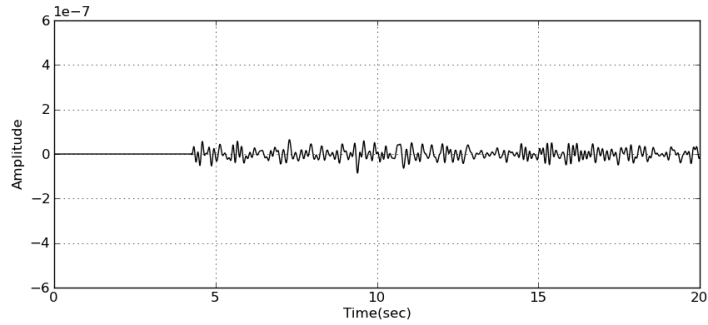
Unlike the random noises in the previous example, coherent noises refer to noises that have consistent phases and amplitudes. Most coherent noises are involved with the characteristics of the subsurface structures, but they are not simulated by the acoustic wave equation, which is a governing equation of the waveform inversion algorithm in this study. Therefore, they act as a hindrance to successful waveform inversion. In the waveform inversion algorithm with an acoustic wave equation, several meaningful seismic events, such as surface waves or mode-converted waves, are also categorized as coherent noises. In this example, hyperbolic noises representing mode-converted waves are added to the noise-free synthesized data based on the numerical experiment performed by Ha et al., (2010b) (Figure 22). Figure 23 is a comparison of an example trace with and without the coherent noises.

Single-damping LWI is performed again using the same 6 damping constants ranging from 1 to 6 s^{-1} for the data contaminated by the coherent noises. The various settings (e.g., initial velocity model, velocity constraint, stopping criterion, and step length) for the inversion are also same as the previous examples. When the single-damping LWI is performed using a damping constant of 1 or 2 s^{-1} , the entire area is also overestimated or underestimated, severely (Figure 24a-b). When the damping constant is 3 s^{-1} , three high velocity areas are identified, but their shapes are completely different from the true velocity model (Figure 24c). In contrast, when the damping constant is larger than or equal to 4 s^{-1} , the inverted velocity models are identical to the results using the noise-free data (Figure 24d-f). The speeds of the elastic wave propagation, such as the surface waves and mode-converted waves, are generally slower than the primary (compressional) wave, so the various elastic effects are recorded later than the acoustic waves. Therefore, in Equation 45, which shows the difference between the logarithmic residuals with and without the noises, $T_n - T_d$ has a positive

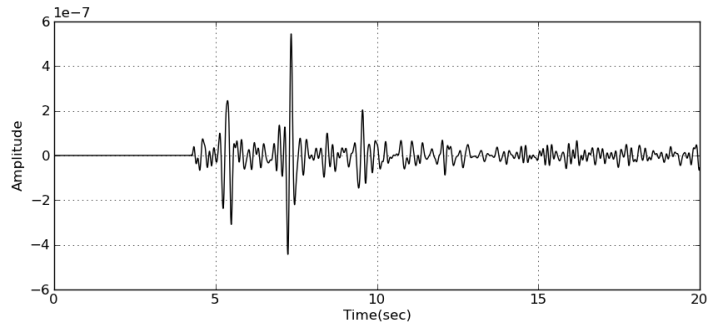
value, and the exponential term containing $T_n - T_d$ rapidly converges to zero when the damping constant s is large enough. In this numerical example, 4 s^{-1} is large enough to cause the noises in the logarithmic residual to approach zero, and the amplitude-level and arrival time of the coherent noises do not degrade the quality of the inverted velocity model.



(a)



(b)



(c)

Figure 18. Time trace of the (a) noise-free observed data (d_{ideal}), (b) pure noise data (n), and (c) the noise-contaminated data ($d_{noisy} = d_{ideal} + n$). In this figure, T_d is equal to T_n assuming random noises

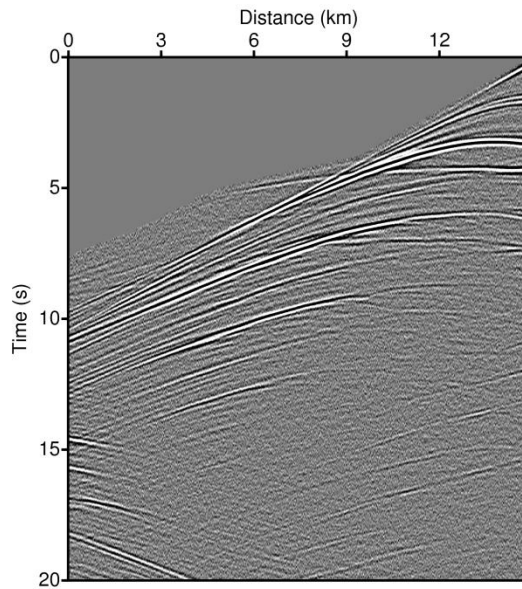


Figure 19. An example common shot gather with random noise where the source is located at 20 km of the velocity model

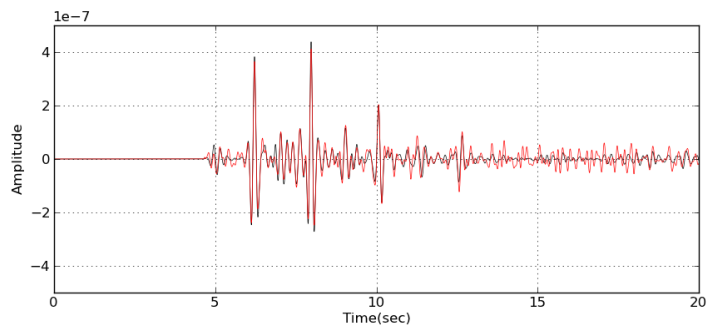


Figure 20. Comparison of the traces at 6km from Figure 19 with (red solid line) and without (black solid line) random noises

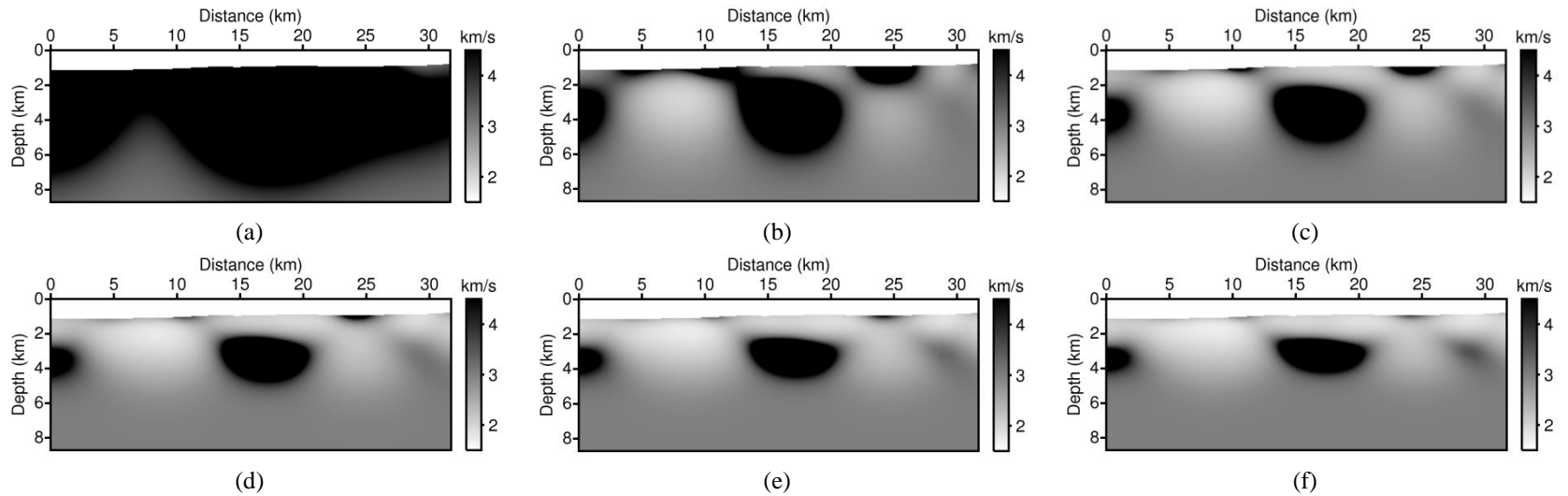


Figure 21. Inverted velocity model obtained by single-damping LWI using a damping constant of (a) 1, (b) 2, (c) 3, (d) 4, (e) 5, and (f) 6 s^{-1} for synthetic data with random noises

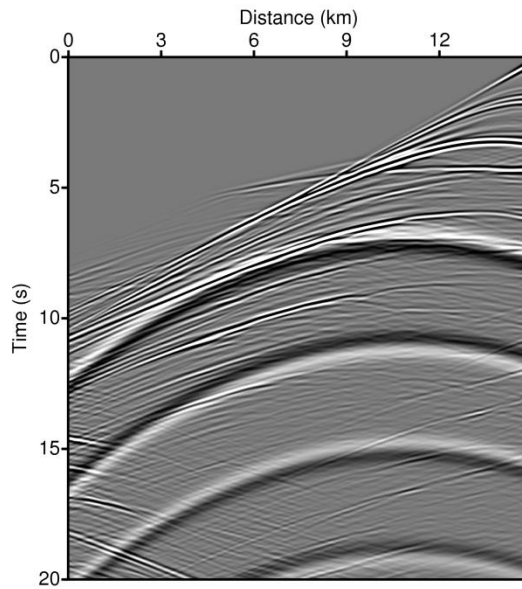


Figure 22. An example common shot gather with coherent noise where the source is located at 20 km of the velocity model

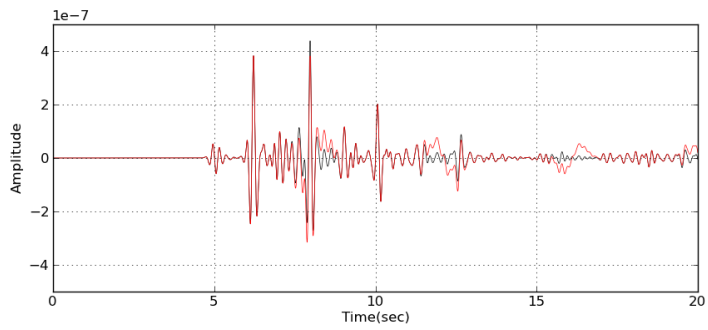


Figure 23. Comparison of the traces at 6km from Figure 22 with (red solid line) and without (black solid line) coherent noises

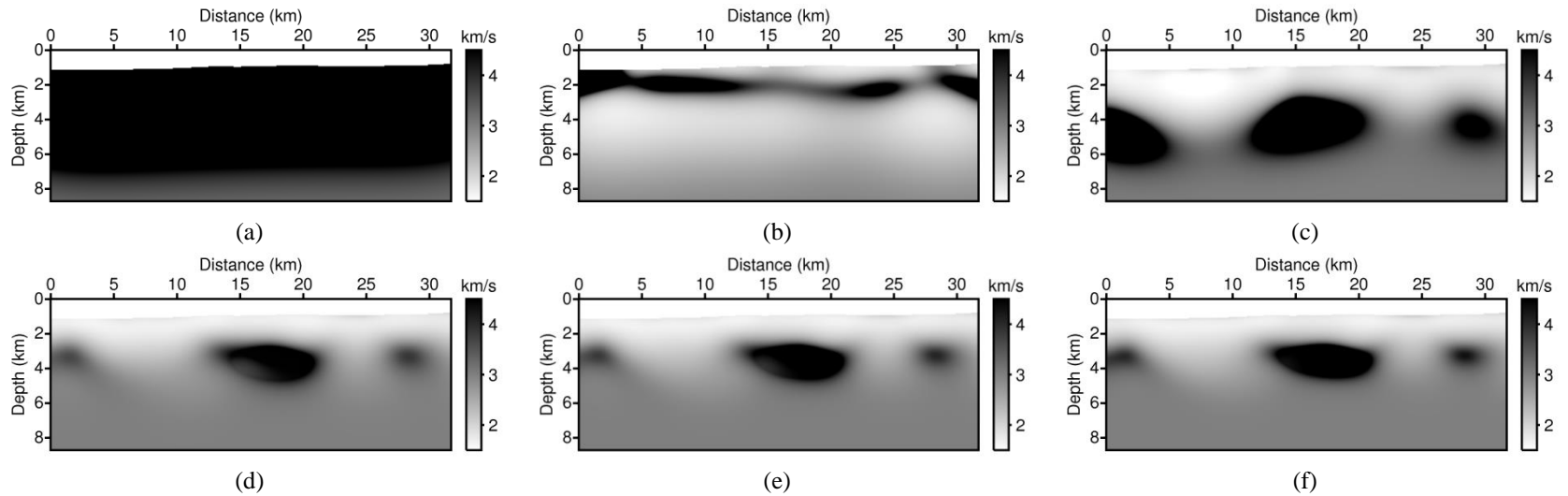


Figure 24. Inverted velocity model obtained by single-damping LWI using a damping constant of (a) 1, (b) 2, (c) 3, (d) 4, (e) 5, and (f) 6 s^{-1} for synthetic data with coherent noise

3.3.3. Ignoring late arrivals

Time traces in the seismic data contain many late arrivals recorded after the first break because of the strong heterogeneity of the subsurface model. However, in this section, the complex time trace is simplified, and it contains only two signals (first and second arrivals) to analyze the effect of the travel time and damping constant on the logarithmic residual. First, the time-domain modeled and observed data with only first and second arrivals are defined as follow:

$$u(t) = f_{u1}(t - T_{u1})H(t - T_{u1}) + f_{u2}(t - T_{u2})H(t - T_{u2}) \quad (46)$$

$$d(t) = f_{d1}(t - T_{d1})H(t - T_{d1}) + f_{d2}(t - T_{d2})H(t - T_{d2}), \quad (47)$$

where $f_{u1}(t)$ and $f_{u2}(t)$ are wavelets of the first arrival and second arrival, and T_{u1} and T_{u2} are those arrival times. In Equation 46, T_{u2} is always larger than T_{u1} . Similarly, $f_{d1}(t)$, $f_{d2}(t)$, T_{d1} , and T_{d2} are those of the observed data. Using the property of Laplace transform on the Heaviside step function, Laplace-domain modeled and observed data can be obtained.

$$\tilde{u}(s) = \tilde{f}_{u1}(s)e^{-sT_{u1}} + \tilde{f}_{u2}(s)e^{-sT_{u2}} \quad (48)$$

$$\tilde{d}(s) = \tilde{f}_{d1}(s)e^{-sT_{d1}} + \tilde{f}_{d2}(s)e^{-sT_{d2}} \quad (49)$$

where $\tilde{u}(s)$, $\tilde{d}(s)$, $\tilde{f}_{u1}(s)$, $\tilde{f}_{u2}(s)$, $\tilde{f}_{d1}(s)$, and $\tilde{f}_{d2}(s)$ represent Laplace-transformed $u(t)$, $d(t)$, $f_{u1}(t)$, $f_{u2}(t)$, $f_{d1}(t)$, and $f_{d2}(t)$.

The logarithmic residual ($\log \tilde{u} - \log \tilde{d}$ or $\log \frac{\tilde{u}}{\tilde{d}}$), which is to be minimized in LWI, can be calculated as

$$\log(\tilde{u}(s)) - \log(\tilde{d}(s)) = \log\left(\frac{\tilde{f}_{u1}(s)e^{-sT_{u1}} + \tilde{f}_{u2}(s)e^{-sT_{u2}}}{\tilde{f}_{d1}(s)e^{-sT_{d1}} + \tilde{f}_{d2}(s)e^{-sT_{d2}}}\right), \quad (50)$$

and it can be decomposed into three terms as follows:

$$\begin{aligned}
& \log(\tilde{u}(s)) - \log(\tilde{d}(s)) \\
&= \log\left(\frac{\tilde{f}_{u1}(s)}{\tilde{f}_{d1}(s)}\right) + \log\left(\frac{1 + \frac{\tilde{f}_{u2}(s)}{\tilde{f}_{u1}(s)} e^{-s(T_{u2}-T_{u1})}}{1 + \frac{\tilde{f}_{d2}(s)}{\tilde{f}_{d1}(s)} e^{-s(T_{d2}-T_{d1})}}}\right) \quad (51) \\
&\quad - s(T_{u1} - T_{d1}).
\end{aligned}$$

To investigate the effect caused by the arrival time of the first and second arrivals on the logarithmic residual, I assume that the wavelet of first arrival in modeled and observed data are the same in both the time and Laplace domain ($f_{u1}(t) = f_{d1}(t)$ and $\tilde{f}_{u1}(s) = \tilde{f}_{d1}(s)$). The wavelets of the second arrival are also assumed to be the same ($f_{u2}(t) = f_{d2}(t)$ and $\tilde{f}_{u2}(s) = \tilde{f}_{d2}(s)$). Then, Equation 51 can be simplified to Equation 52:

$$\log(\tilde{u}(s)) - \log(\tilde{d}(s)) = s(T_{d1} - T_{u1}) + \log\left(\frac{1 + e^{-s(T_{u2}-T_{u1})}}{1 + e^{-s(T_{d2}-T_{d1})}}\right) \quad (52)$$

Under the assumption of the same shape of the wavelet, the logarithmic residual can be represented as a function of only the travel time and damping constant. In Equation 52, the first term on the right hand side is a term representing the residual calculated from the difference between the arrival times of the first arrivals in the modeled and observed data, and the second term is the residual calculated from the intervals between the first and second arrivals in the modeled and observed data. The first term is linear with the size of the Laplace damping constant and the difference in the first arrival times. However, the exponential functions in the second term converge to 0 when the intervals between the first and second arrivals are large and a large damping constant is used, which leads to the minimized second term.

As Equation 52 shows, the logarithmic objective function in the Laplace domain updates the velocity model by minimizing only the difference between the travel times of first breaks in the modeled and observed data. Thus, it is going to be very similar to the first-arrival travel time tomography algorithm, which considers only the first arrived refracted signals by ignoring all late arrivals, and it inverts the very shallow part of the model (e.g., one fourth of the maximum offset).

3.3.4. Exceeding the threshold in floating point operations

The computer calculation using large damping constants is not robust for the Laplace transform of the time-domain data because it might produce Laplace-domain signals that are equal to 0, especially for the large-offset data. Figure 25 shows Laplace-transformed time-domain data (Figure 5) using 5 large damping constants between 7 and 15 s⁻¹ at an interval of 2 s⁻¹. In this figure, the Laplace-domain data decay faster as the distance from source increases; this effect is more significant when the damping constant is large. The minimum real value recognized by the single-precision computer program is 10⁻³⁸. In Figure 25, the values smaller than black solid line (10⁻³⁸) are recognized as 0 by the single-precision waveform inversion program. The far-offset data usually contain more information, which is necessary for constructing the long-wavelength velocity model. However, for large damping constants, we lose a large amount of information in the far offset, and which severely constrains the correct inversion of the long-wavelength velocity model.

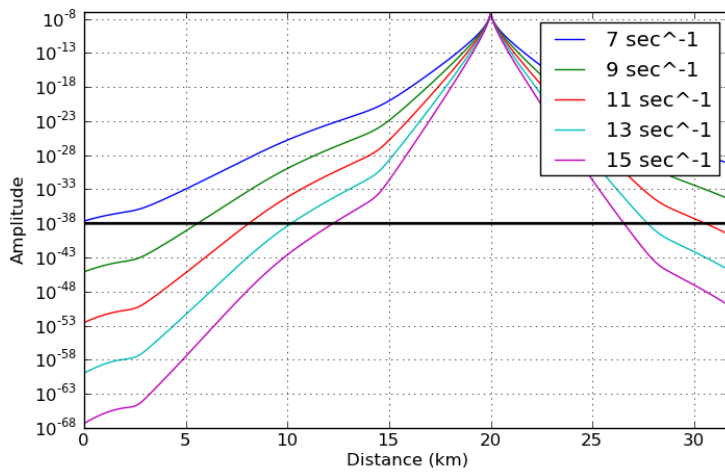


Figure 25. Synthetic common shot gather in the Laplace domain for five large damping constants (7, 9, 11, 13, and 15 s^{-1}). The thick black solid line is the minimum value (10^{-38}) that can be represented in the single-precision waveform inversion program

3.4. Range for proper damping constants for single-damping LWI

In this study, LWI using only a single damping constant is suggested. To accomplish this goal, I am faced with the problem of selecting the best damping constant to use for single-damping LWI that yields the best inversion result. However, due to the diverse conditions of seismic data acquisition (e.g., maximum and minimum offset, maximum listening time, survey distance, and effects of noises) and geological background (e.g., distribution of velocity component and depth of the water layer), it is impractical to define the most optimum single damping constant that covers all possible cases. Instead of selecting a single value for the damping constant, a range for the proper damping constant for single-damping LWI is suggested by considering the results of numerical experiments performed using the reference synthetic data generated by the Pluto 1.5 velocity model. Small damping constants can invert the macro area including the deep part of the model, but they result in low resolutions of the inverted velocity model (section 3.2). In addition, small damping constants show severe weakness in inverting the Laplace-transformed time-domain observed data when they have short listening time or they are contaminated by several types of noise (section 3.3). In contrast, large damping constants show higher resolutions compared to the small damping constants show, but the imaging depth is excessively restricted (section 3.2). Based on these numerical examples, I suggest a range of proper damping constants for single-damping LWI is from 5 to 9 s⁻¹. As confirmed in section 3.2, the inverted velocity models using these damping constants are similar enough to each other that the maximum difference due to the relative model misfit is smaller than 0.5. In addition, they are robust with respect to the effects caused by the short-listening time and various unwanted signals such as random noises and coherent noises.

3.5. Accuracy of single-damping LWI using a depth weighting function

Even though the theoretical background of the role of various damping constants is not firmly established, empirically selected multiple damping constants ranging from 1 to 15 s⁻¹ at an interval of 1 or 2 s⁻¹ are commonly used by the conventional LWI algorithm. The reason is based on the different behavior of the sensitivity kernel in the waveform inversion algorithm for different damping constants, and it was analyzed by Bae et al., (2012). A single damping constant among the medium range of damping constants can be used to generate similar results to the conventional LWI algorithm, but there is a risk that only a certain area of the model will be overestimated while the other areas will be updated less because of the locally positioned sensitivity kernel of a certain damping constant. In the 3-D magnetic and gravity data inversion algorithm, an exponentially increasing depth weighting function is used to counteract the natural decay of the kernels so that the inversion yields better depth information (Li and Oldenburg, 1998, 1996). In this study, the depth weighting functions that are used by the 3-D magnetic and gravity data inversions are modified to enhance the quality of the inverted model of single-damping LWI.

First, one of the medium range damping constants is used to compute the gradient directions for the entire area. Subsequently, the final scaled gradient directions are calculated using the original gradient direction for a single damping constant and various depth weighting functions as follows:

$$\hat{\mathbf{g}} = \mathbf{NRM} \left\{ \sum_{i_{scale}=N_1}^{N_2} \mathbf{NRM}\{\mathbf{g}^{i_{scale}}\} \right\}, \quad (53)$$

where

$$\mathbf{g}_{k(ix,iy,iz)}^{i_{scale}} = \frac{\partial E(\mathbf{m})}{\partial m_{k(ix,iy,iz)}} \times iz^{i_{scale}}. \quad (54)$$

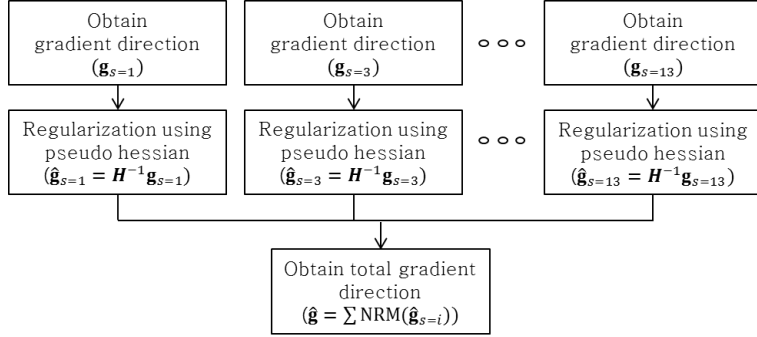
In Equation 53 and 54, $\frac{\partial E(\mathbf{m})}{\partial m_{k(ix,iy,iz)}}$ is the original gradient direction of the k -th element (where ix , iy , and iz are its grid indexes in the x , y , and z directions); $\mathbf{g}^{i_{scale}}$ is the scaled gradient direction using i_{scale} as the scaling index; $\hat{\mathbf{g}}$ is the final gradient direction, which is a summation of several $\mathbf{g}^{i_{scale}}$; and **NRM** is the normalization operator, which adjusts the maximum absolute value to 1 to equally constrain the contributions of each damping constant. The scaling method using depth weighing functions can be regarded as a method that approximates the gradient of the conventional algorithm (using various damping constants) by applying various depth weighting functions (i.e., varying with respect to the depth index) to the gradient of the proposed single-damping LWI algorithm. In this study, N_1 is -3 and N_2 is 3, so 7 different depth weighting functions are applied to the original gradient that is obtained using a damping constant of 7 s^{-1} . When i_{scale} is a negative number, it emphasizes the shallow part of the gradient, and it can be thought of as approximating the use of a large damping constant. Inversely, when i_{scale} is a positive number, it emphasize the deep part of the gradient, and it can be thought of as approximating the use of small damping constant. The diagram for this approximation is illustrated in Figure 26. This scaling method with a depth weighting function and the weighting indexes N_1 and N_2 are obtained empirically through the various numerical experiments in this study for the case using 7 s^{-1} as a single damping constant. Therefore, the development of a more sophisticated scaling method is left to be introduced in future studies.

A numerical test is performed to show the validity of the proposed scaling method for single-damping LWI with a damping constant of 7 s^{-1} . First of all, the conventional LWI is performed to generate the reference inverted velocity model. In this study, the method inverting the Laplace-domain wave field for 7 damping constants from 1 to 13 s^{-1} at an interval of 2 s^{-1}

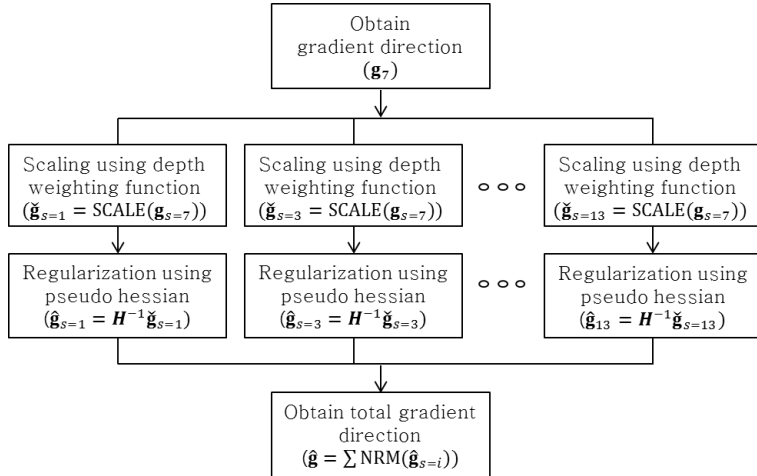
simultaneously is defined as the conventional LWI. Figure 27 is the reference inverted velocity model, and it shows the correct long-wavelength structure of the true velocity model for the entire part of the model by inverting the wave field for various damping constants. Subsequently, single-damping LWI with the scaling method is performed for a damping constant of 7 s^{-1} (Figure 28). In this example, the result, which the scaling method is applied, is similar to the case which is regularized only by the pseudo Hessian (Figure 11g). However, it shows improvements in the deep part of the high velocity area and produces a more balanced inverted velocity model with respect to the depth axis. In addition, by calculating the relative model misfit using Equation 21 with the reference inverted velocity model (Figure 27), we can confirm that the scaling method using a depth weighting function provides more analogous result to that of the conventional LWI using various damping constants for single-damping LWI (Figure 29).

The main objective of the LWI is providing a nice initial velocity model for the subsequent frequency-domain waveform inversion or time-domain waveform inversion. The solutions of the frequency-domain and time-domain waveform inversions tend to converge to the one of many local minima because of the phase wrapping and cyclic-skipping problems, respectively (Bunks et al., 1995; Sirgue and Pratt, 2004), especially when the initial velocity model is not good. Therefore, we perform the frequency-domain waveform inversion to verify the inverted velocity model obtained by single-damping LWI algorithms. For the frequency-domain waveform inversion algorithm, 24 discrete frequencies from 1.25 to 7.0 Hz at an interval of 0.25 Hz are used. The conventional l_2 objective function is used with the pseudo Hessian matrix for the regularization (Shin et al., 2001). The maximum number of iterations is defined as 200 with a fixed step length of 50 m/s. During the inversion, the velocity at the water layer is fixed at 1,500 m/s without updating, and the updated velocity model is constrained between 1,500 and 4,514 m/s.

Before using the result of LWI as the initial guess, the two-layered homogeneous velocity model and the linear gradient velocity model with a water layer are used for the initial velocity model to identify problems that can be caused by a bad initial velocity model. Figure 30a and Figure 30b show the frequency-domain inverted velocity model using the two-layered homogeneous and linear gradient models as initial guess, respectively. Even though the low frequency components of the synthetic seismic data are used for the inversion (the lowest frequency is 1.25 Hz), the inverted velocity model is still far from the true velocity model in both cases. When using the two-layered homogeneous velocity model as an initial guess, a large number of artifacts are identified in the shallow parts of the model below the sea floor. When using the linear gradient velocity model, the shallow parts of the inverted velocity model are acceptable, but the subsalt structure is not inverted at all. For both cases, the velocities inside the salts are not inverted at all. In contrast, Figure 31a and Figure 31b, which are the frequency-domain inverted velocity models using the results of conventional and single-damping LWI, respectively, show good agreement with the true velocity model. Short and medium wavelength structures are added to the background smooth velocity models, so the three salt structures are correctly inverted and the fine layered structures are also clearly identified for the entire area. In addition, the difference between these two velocity models is undetectable to the naked eyes despite the initial models are slightly different. Therefore, it is concluded that the result of single-damping LWI is as good as that of the conventional LWI to be used as initial velocity models for subsequent frequency-domain waveform inversion.



(a)



(b)

Figure 26. Diagrams for (a) conventional LWI using various damping constants and (b) proposed single-damping LWI using a scaling method with a depth weighting function

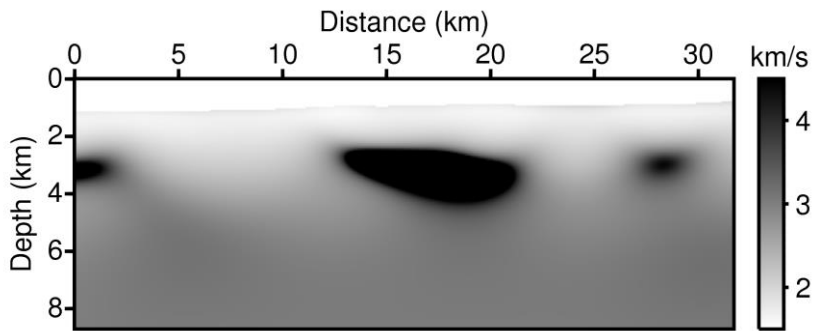


Figure 27. Inverted velocity model obtained using conventional LWI

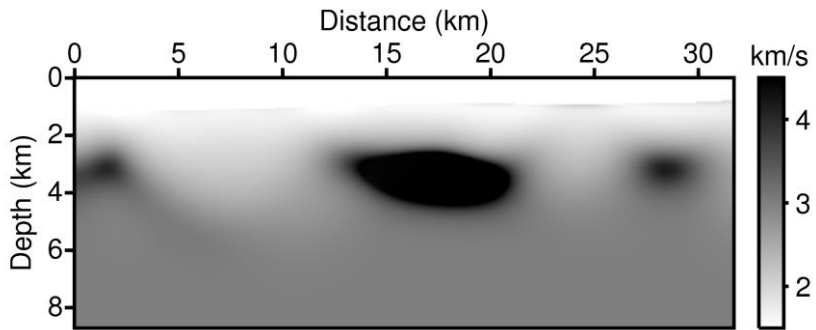


Figure 28. Inverted velocity model obtained using single-damping with the depth weighting function using a damping constant of 7 s^{-1}

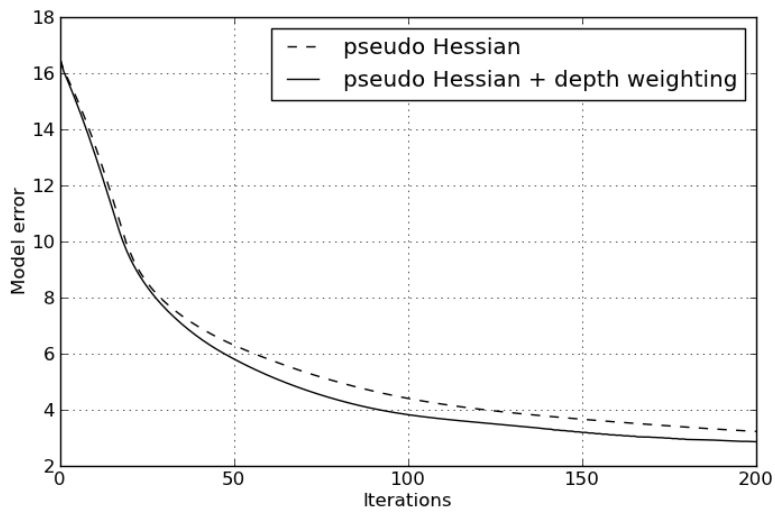
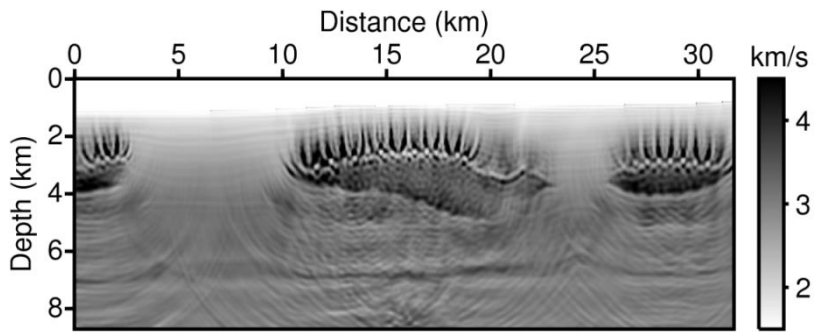
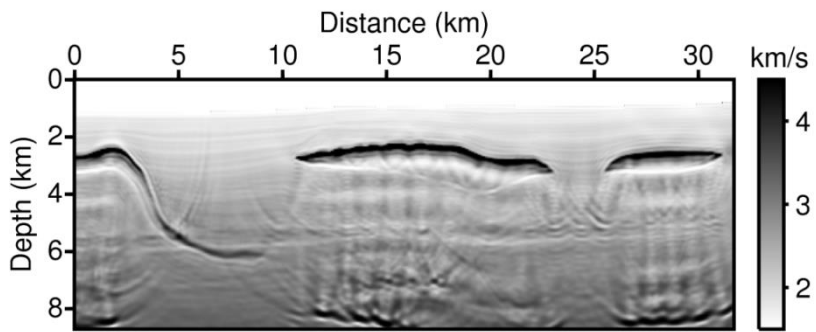


Figure 29. History of the relative model misfit between the inverted velocity model using conventional LWI and inverted velocity model using single-damping LWI regularized by pseudo Hessian only and regularized by pseudo Hessian and depth weighing using a damping constant of 7 s^{-1}

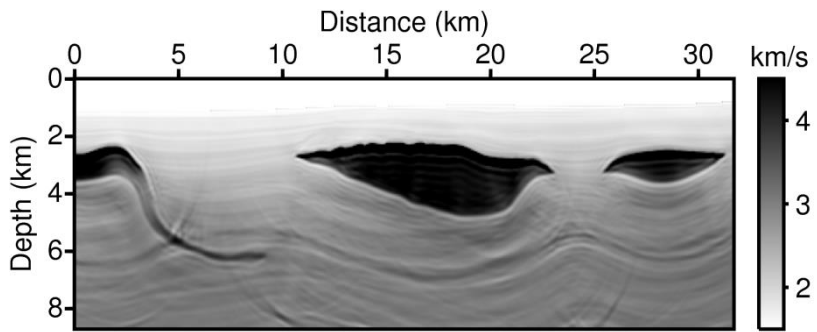


(a)

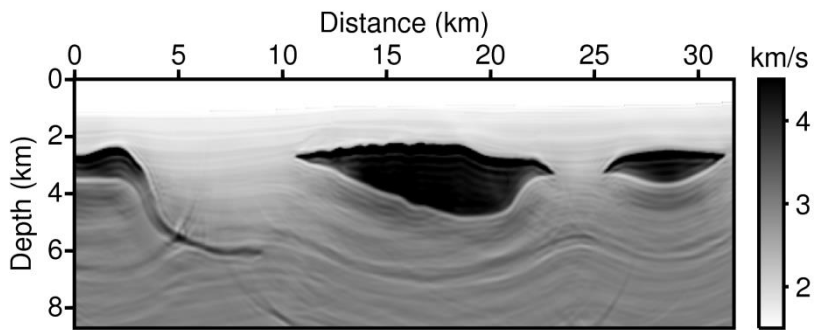


(b)

Figure 30. Inverted velocity models in the frequency domain using the (a) two-layered homogeneous and (b) linear gradient velocity models as the initial velocity model



(a)



(b)

Figure 31. Inverted velocity models in the frequency domain using the result of (a) conventional LWI and (b) single-damping LWI as an initial velocity model

3.6. Computational efficiency of single-damping LWI

The enhanced computational efficiency is the biggest advantage of single-damping LWI over conventional LWI. In the LWI algorithm using a direct matrix solver, the total number of floating point operations is proportional to the number of damping constants because each damping constant constructs an independent impedance matrix and most computing operations are involved in matrix factorization and solving. Therefore, choosing a small number of damping constants directly leads to a reduction in the total number of computing operations.

Conventional LWI using various damping constants is generally performed using a cluster of CPU cores through parallel computer programming. In the parallelized inversion algorithm, each CPU core is assigned to a different damping constant and constructs an impedance matrix and decomposes it into lower and upper matrix factors (Golub and Loan, 1996). Subsequently, each CPU core calculates the forward and adjoint (backward) wave field by applying the forward and backward substitution of the lower and upper matrix factors to a number of source and residual vectors. Finally, the gradient directions are constructed for each damping constant. The exclusive role of the master core is summing the gradients constructed from all damping constants and updating the summed gradient to the previous velocity model using a proper step length. In the single-damping LWI algorithm, parallelization can be applied with respect to the different source positions not to the different damping constants. Therefore, we can achieve an additional enhancement of the computing efficiency by using the same number of CPU cores and the single-damping LWI algorithm.

When using only a single CPU core for both the conventional and single-damping LWI algorithms, the computing time of single-damping LWI is faster by as much as the number of damping constants used for the conventional LWI. This is obviously straightforward, so the analysis of the computing

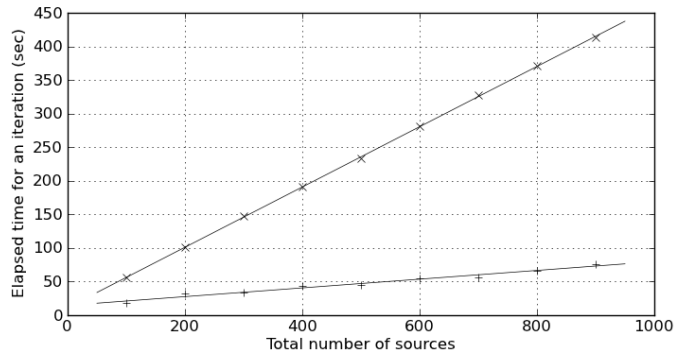
efficiency for this case is not performed in this study. Furthermore, the minimum unit of CPU cores for a typical workstation or CPU cluster is larger than four (in quad-core processors) or eight (in octa-core processors) under the current computing environments; therefore, it is impractical to execute the inversion program using a single CPU core.

In this study, the elapsed computing time for an iteration using the same synthetic data are measured using the conventional and single-damping LWI algorithm by changing the grid interval and the total number of sources. The degree of freedom of the impedance matrix is same as the total number of nodal points when a 2nd-order acoustic wave equation is used. Therefore, we can change the size of the matrix using the three different grid intervals without changing the imaging area. The degree of freedom of impedance matrix using the grid interval of 25 m, 50 m, and 100 m is 733,941, 184,096, and 46,024, respectively. The total number of sources is also increased from 100 to 900 at an interval of 100 to investigate the efficiency enhancement with respect to the total number of sources. When the forward and backward substitution is performed using the lower and upper matrix factors for the right hand side vectors (e.g., source vectors for forward modeling and residual vectors for adjoint modeling), several right hand sides are grouped, and the multi-column right hand sides are formulated for the better efficiency. In this example, 25 source vectors are grouped for the forward modeling, so the total number of source groups increases from 4 to 36 with an interval of 4. The same grouping is also performed for the residual vectors in the backward modeling. To factorize and solve the impedance matrix, the DMS multi-frontal matrix solver package is adopted (Kim and Kim, 1999).

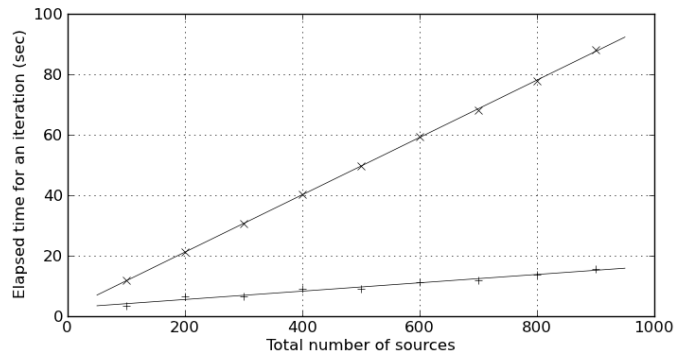
Figure 32 shows the elapsed time for an iteration with respect to the total number of source positions using three different grid intervals of 25 m, 50 m, and 100 m. The \times marks represent the elapsed time of the conventional LWI using 7 damping constants achieved by 7 CPU cores, and it shows that the total elapsed time linearly increases with the number of source positions. The

+ marks represent the elapsed time of the single-damping LWI achieved by 7 CPU cores. Inverting more sources requires longer computational time, but it does not strictly follow the linear trend as in the case of conventional LWI because the number of source groups (4, 8, 12, ..., 36) is not always divided by the number of CPU cores, so the load for each CPU core is not equally distributed. However, when the linear trend is plotted, 9 samples from 100 to 900 do not show large deviations from the linear trend as the number of sources increases.

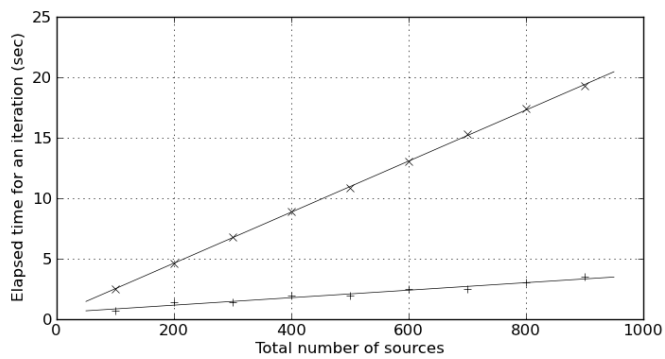
To calculate the speedup of the proposed single-damping LWI over conventional LWI using 7 CPU cores, I compute the ratio of the linear trends of the \times marks and the + marks. In Figure 33, three lines representing the speedups of the single-damping LWI over the conventional LWI are very similar to each other for all three different grid intervals. This means that the size of the impedance matrix does not severely affect the computing efficiency obtained by the single-damping LWI algorithm even though it affects the absolute computing time for all cases. However, the speedup of the single-damping LWI is deeply related to the total number of sources. For a larger number of sources, it shows the higher efficiency, but the speedup is going to converge at a certain point assuming an infinite number of sources. This can be explained by two reasons: 1) As the number of shot groups increases, the load for each CPU core is more equally distributed, and 2) as the number of shot groups increases, the portion of the matrix factorization that is not a parallelized part of the algorithm is less dominant.



(a)



(b)



(c)

Figure 32. Elapsed time for an iteration with respect to the total number of sources when the grid interval is (a) 25, (b) 50, and (c) 100 m using 7 CPU cores. The \times marks represent the elapsed time of conventional LWI, and the $+$ marks represent the elapsed time of single-damping LWI. The linear trend lines are plotted with black solid lines using 9 samples for all cases

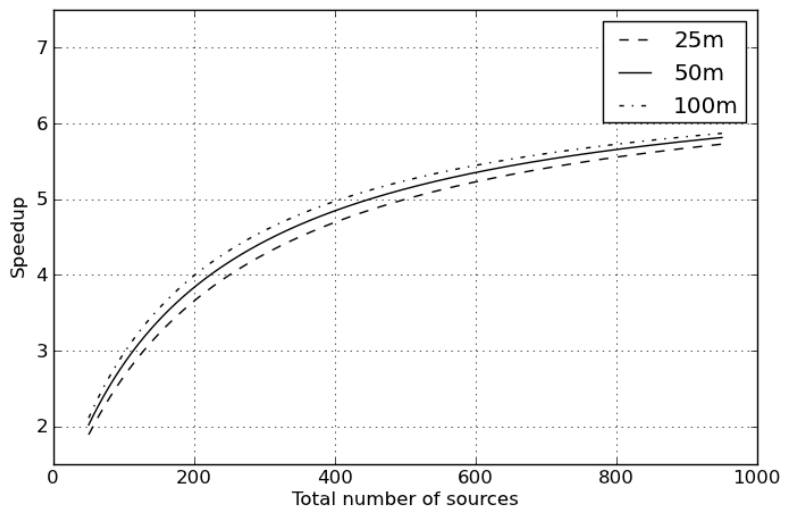


Figure 33. Speedup of the proposed single-damping LWI algorithm compared to the conventional LWI algorithm using the linear trend lines calculated from the 9 discrete samples in Figure 32

4. Real dataset example

In this section, 2-D real data are used to verify the proposed single-damping LWI algorithm by comparison with the conventional LWI algorithm. Firstly, I briefly introduce the acquisition geometry of the real data and the preprocessing procedure for LWI. Subsequently, several options for the waveform inversion are introduced, and the conventional and single-damping LWI are applied to the real data under identical conditions. I do not have the true subsurface velocity model of the field where the real data are obtained. Therefore, reverse time migration is performed to investigate the accuracy of the inverted velocity model. Additionally, the synthetic common shot gathers are generated in both the Laplace and time domains using the inverted long-wavelength velocity model to verify the proposed LWI algorithm.

4.1. Preprocessing for the Laplace-domain waveform inversion

To acquire the TOTAL data, 1,156 sources are used with 37.5-m source spacing, so the total survey area is 43.3 km. In the survey area, the sea floor varies from 96 m to 1,588 m, which indicates that the survey is performed in an offshore environment. Each source contains 804 receivers, and the first and last receivers are 165 m and 10,202 m away from the source. Each receiver records the pressure wave field for 12 s with a sampling interval of 0.004 s. As preprocessing stages, band pass (low-cut) filtering is applied to remove the noise in the low frequency ranges (0 ~ 5 Hz), and muting before the first signal is performed before applying the Laplace transform to the data. The various preprocessing stages for real data application of LWI is well illustrated by Ha et al., (2012a).

Figure 34 shows an example of a common shot gather in the time domain for the 601st source, which is located at 24 km of the imaging area, Figure 35 shows its frequency spectrum. As Figure 35 shows, the dominant frequency ranges from 15 to 60 Hz, and there are no low frequency components below 5 Hz, which were already removed by the band pass (low-cut) filtering. Finally, the preprocessed time-domain data are transformed into the Laplace domain using 7 damping constants from 1 to 13 s⁻¹ at an interval of 2 s⁻¹. Figure 36 shows Laplace-domain common shot gathers for three different damping constants (3, 7, 11 s⁻¹). The ideal Laplace-domain wave field obtained by the acoustic wave equation is not supposed to contain high wavenumber components irrespective of the complexity of the velocity model. In contrast, the Laplace-transformed real data contains many high wavenumber contents for several reasons (e.g., random noise, instrumental noise, acquisition geometry, elastic noises, and among other reasons). These high wavenumbers can be observed more easily when the damping constant is smaller. However, these high-wavenumber components in the observed data do not affect the results of Laplace-domain waveform inversion because the Laplace-domain modeling operator serves as a low-wavenumber pass filter and high-

wavenumber components in the observe data are damped out in the adjoint wave field modeling (Ha and Shin, 2013). Laplace-transformed observed data occasionally have extremely small amplitudes, which might cause numerical instability when calculating the logarithmic residual, but this issue can be solved using the filtering technique (Kim et al., 2009).

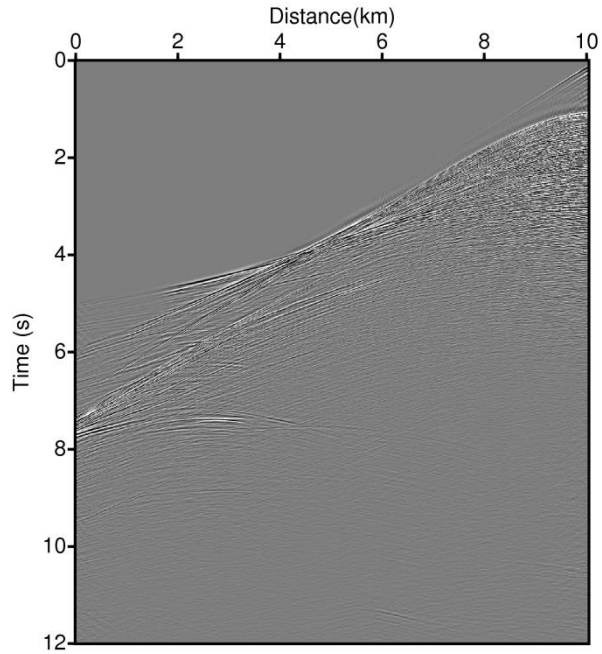


Figure 34. An example common shot gather when the source is located 24 km of the imaging area

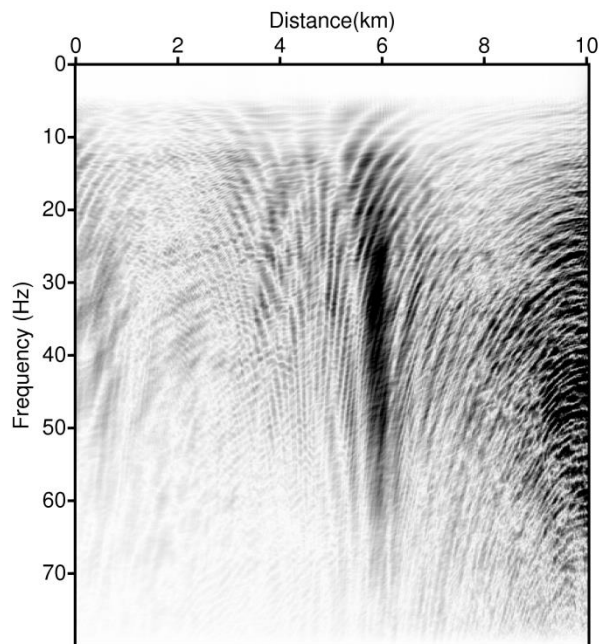
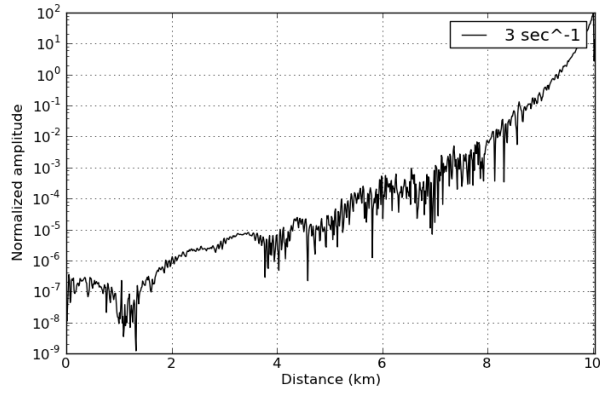
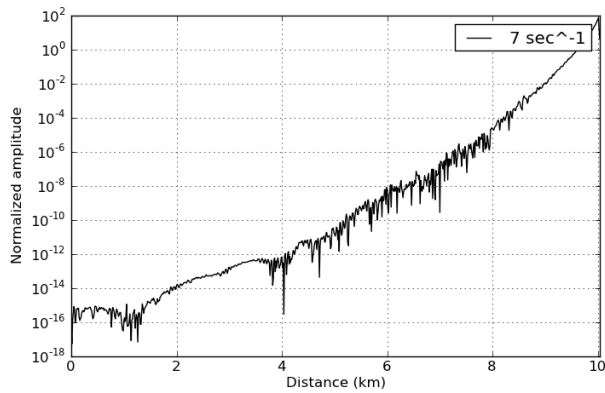


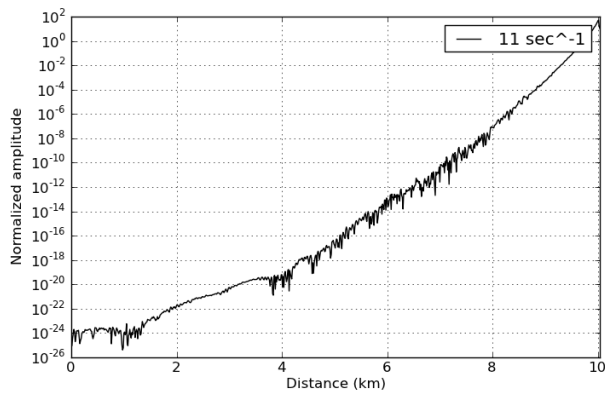
Figure 35. Frequency spectrum of the example common shot gather



(a)



(b)



(c)

Figure 36. Laplace-domain common shot gather when the damping constant is (a) 3, (b) 7, and (c) 11 s^{-1} when the source is located 24 km of the imaging area

4.2. Accuracy of the inverted velocity model

The long-wavelength velocity model is obtained by conventional LWI and single-damping LWI using the TOTAL dataset. The imaging area is 46.3 km, which is extended 1500 m to the left and right of the source range. The imaging depth is set to 6 km. For the spatial discretization, a 25-m uniform grid interval is used for the horizontal and vertical directions, so the total computational dimension of the velocity model is 1852 x 240. The two-layered homogeneous velocity model is used as the initial velocity model (Figure 37). For the stopping criterion, the maximum number of iteration is defined as 200 with a fixed step length of 50 m/s. For the conventional LWI, 7 damping constants from 1 to 13 s⁻¹ with an interval of 2 s⁻¹ are used. For single-damping LWI, a single damping constant of 7 s⁻¹ is used. In both approaches, the velocity at the water layer is fixed to 1,500 m/s without updating, and the velocity updates are constrained between 1,500 and 5,000 m/s.

Figure 38a and Figure 38b show the velocity models obtained by the conventional LWI and single-damping LWI, respectively. Even though the simple two-layered homogeneous model is used as an initial guess, a low-velocity sediment layer in the shallow part and high-velocity salt structures beneath the shallow part are inverted for both cases. Considering only the shallow part of the model between 0 and 4 km deep, both method produce very similar results. However, the parts of the inverted velocity models deeper than 4 km differ from each other; this result can be interpreted as indicating that conventional LWI focuses more on shallower parts than single-damping LWI because of the redundancy of the contributions by large damping constants or that single-damping LWI overestimates the deeper part of the model without properly considering the late arrivals coming from the deeper parts of the model. In addition, it seems that all salt structures are slightly connected in conventional LWI result, but they are separated in the single-damping LWI result. Nevertheless, the overall shapes of the two long-wavelength velocity models are comparable in general. Therefore, it can be

concluded that single-damping LWI produces an inverted velocity model with a similar quality and enhances computing efficiency. However, the detailed difference between two velocity models cannot be judged at the present, and additional analysis should be performed.

The long-wavelength velocity model obtained by LWI can be used as the background velocity for the reverse time migration algorithm (Baysal et al., 1983; McMECHAN, 1983; Whitmore, 1983). Similar to the FWI, reverse time migration is based on full (two-way) wave equations, and it can depict any direction of wave propagation. Therefore, reverse time migration produces the correct subsurface images when the background velocity model is correct. There are various algorithms for the reverse time migration with respect to the wave modeling domains and imaging conditions. In this study, the frequency-domain reverse time migration using the virtual source imaging condition with the source estimation technique is exploited (Kim et al., 2011b). Figure 39 is the brute migrated image using the two-layered homogeneous velocity model that is used as the initial model for LWI (Figure 37), and Figure 40a and Figure 40b are the migrated images using the long-wavelength velocity models obtained from conventional and single-damping LWI, respectively. Compared to the brute migrated image, both migrated images using the inverted velocity models clearly show the layers and faults in the low velocity zone and the tilted layers in the shallow parts of the models. In addition, the boundaries of the high-velocity zones, which are not focused in the brute migrated image at all, are well delineated using the inverted velocity model.

The primarily objective of LWI is minimizing the difference between the logarithmic wave fields (logarithmic residual) between the Laplace-domain observed and modeled data by updating the long-wavelength components of the subsurface velocity model (Equation 5). To confirm whether the difference in the logarithmic wave field is minimized, the Laplace-domain observed and modeled data are compared for the 301st, 601st, and 901st source positions. In

Figure 41-Figure 43 (a), (b), and (c) show comparisons of the logarithmic wave fields for three different damping constants of 3, 7, and 11 s^{-1} using conventional LWI. When the conventional LWI algorithm is used, the modeled data using the inverted velocity model follow the low-wavenumber trend of the observed data compared to the modeled data using the initial velocity model for three different damping constants of 3, 7, and 11 s^{-1} . In the same figures (Figure 41-Figure 43), (d), (e), and (f) show the same comparison using the single-damping LWI, and we can see that the modeled data using the results from single-damping LWI are almost identical to those using the results from conventional LWI even though the modeled data using damping constants of 3 and 11 s^{-1} are not inverted directly by the single-damping LWI. This indicates that the logarithmic residuals in the Laplace domain for various damping constants can be successfully minimized by inverting only a single damping constant.

By comparing the time-domain wave field using the Laplace-domain inverted velocity model, the role of LWI can be understood more intuitively rather than by comparing the Laplace-domain wave field. In Figure 44-Figure 46, (a) is the observed data, (b) and (c) are the modeled data using the inverted velocity model obtained by conventional LWI and single-damping LWI, respectively, for the 301st 601st and 901st source positions. The observed data in the time domain show complex features where various reflected, refracted, and diffracted waves coexist. In contrast, the modeled data using the Laplace-domain inverted velocity model are much simpler. However, the direct wave and first reflection are the same as in the observed data, and the kinematics of the head wave is inverted exactly. In addition, later arrivals including several major events in the observed data can also be seen in the modeled data. By matching a few major events, which are more related to the long-wavelength structure of the subsurface model, LWI mitigates the cycle-skip problem in the time-domain waveform inversion and aids converging to the global minimum.

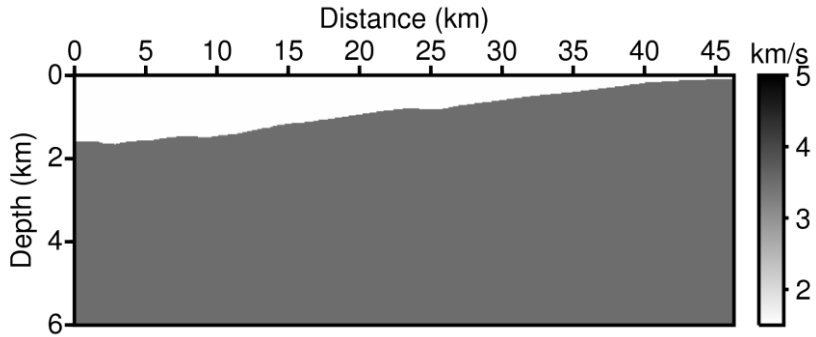


Figure 37. The two-layered homogeneous velocity model for Laplace-domain waveform inversion

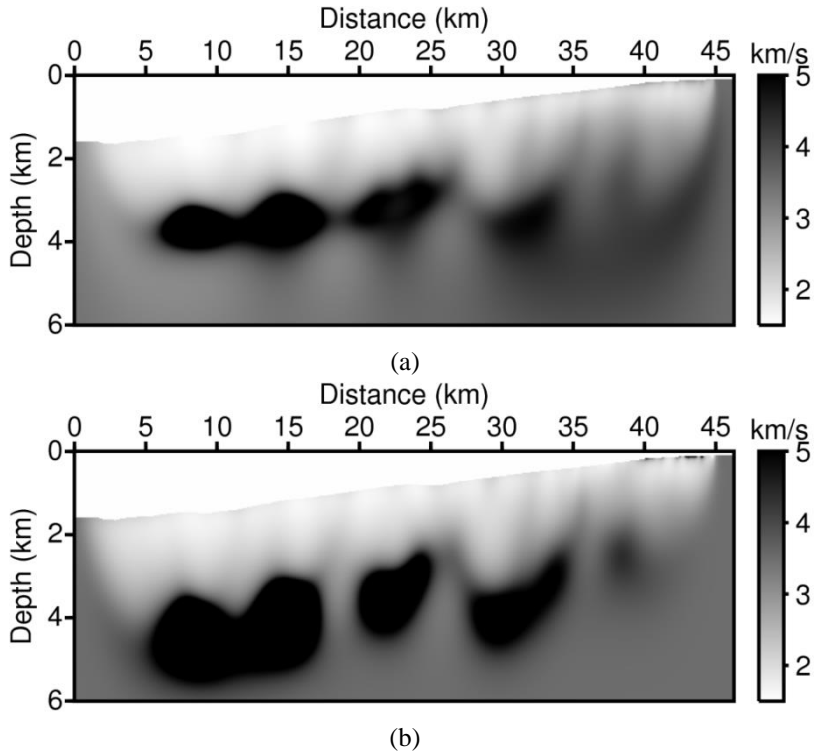


Figure 38. Inverted velocity model obtained by the (a) conventional LWI using 7 damping constants from 1 to 13 s^{-1} at an interval of 2 s^{-1} , and (b) single-damping LWI with depth weighting function using a damping constant of 7 s^{-1}

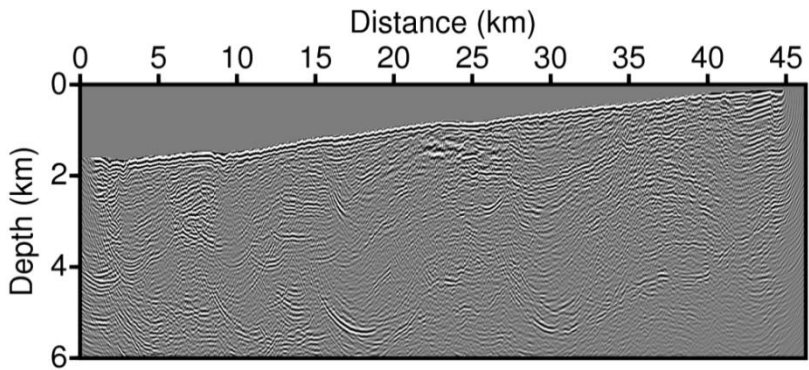
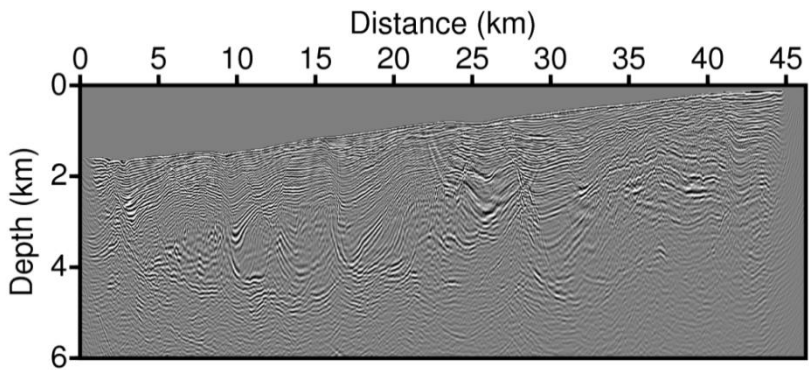
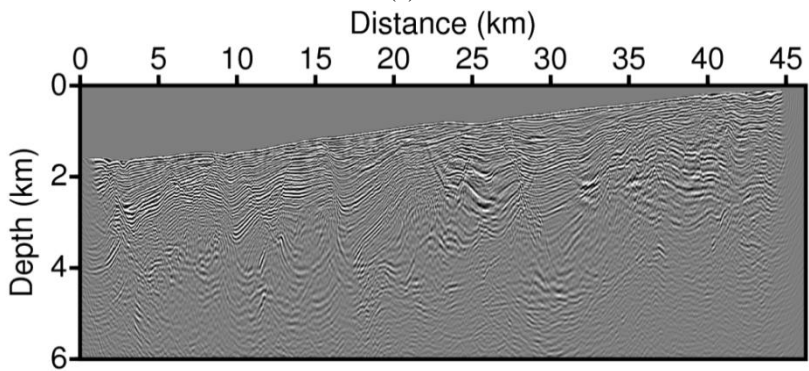


Figure 39. Brute migrated image from the frequency-domain reverse time migration algorithm using the two-layered homogeneous velocity model

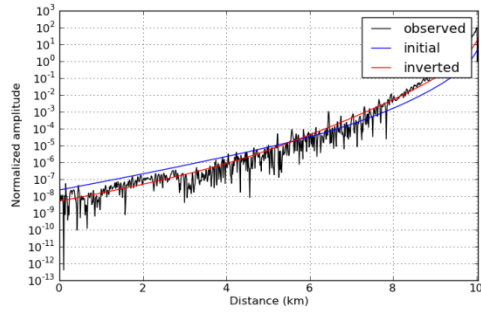


(a)

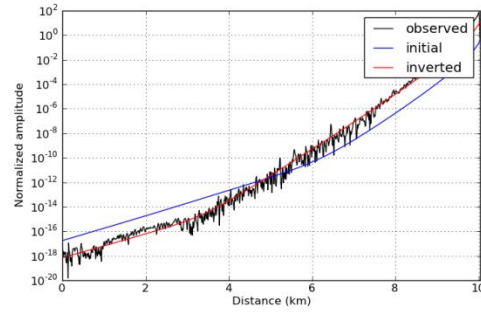


(b)

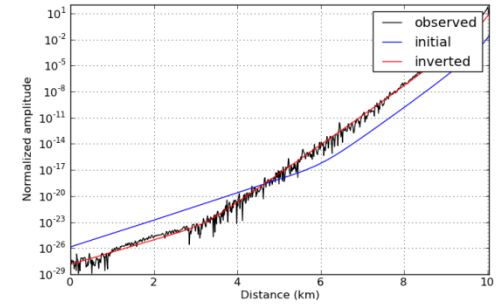
Figure 40. Migrated image from the frequency-domain reverse time migration algorithm using the result of (a) conventional LWI and (b) single-damping LWI



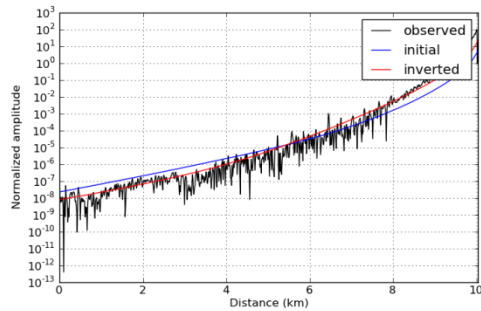
(a)



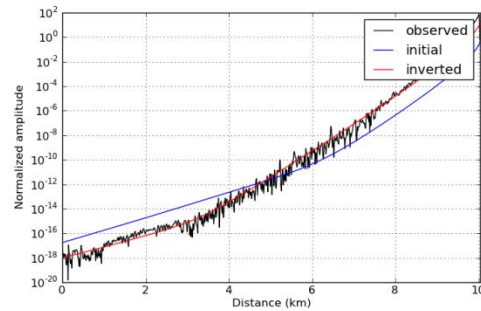
(b)



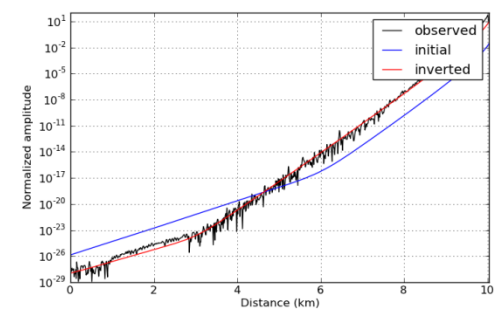
(c)



(d)

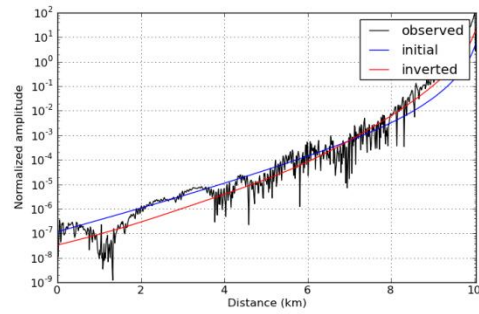


(e)

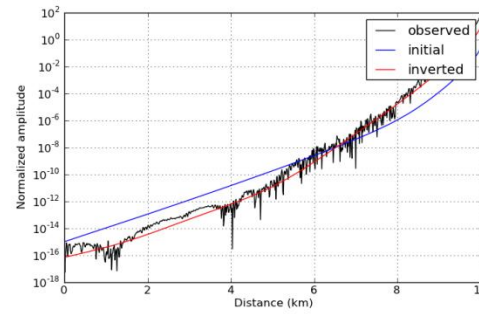


(f)

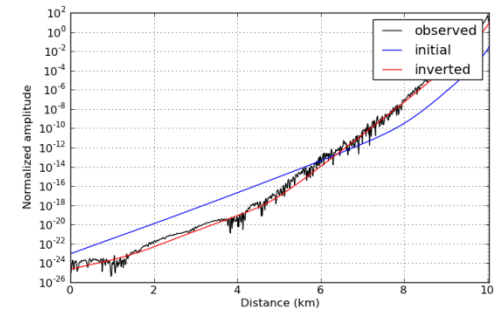
Figure 41. Comparison of the Laplace-domain observed and modeled data at the 301st shot position using the conventional LWI result with damping constants of (a) 3, (b) 7, and (c), 11 s^{-1} . (d), (e), and (f) are the same comparison as (a), (b), and (c) using the single-damping LWI result



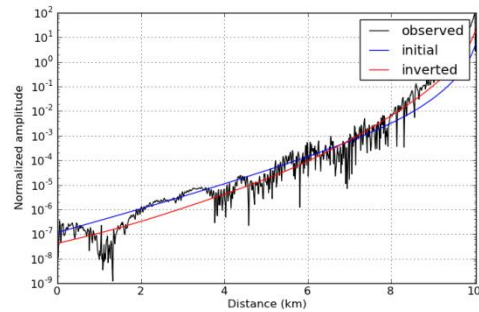
(a)



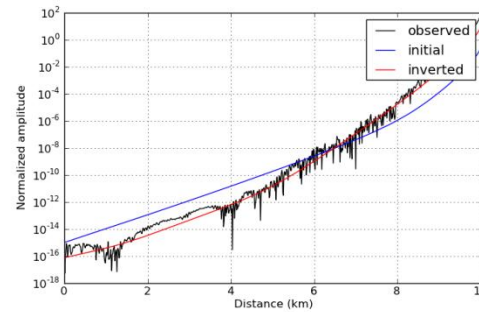
(b)



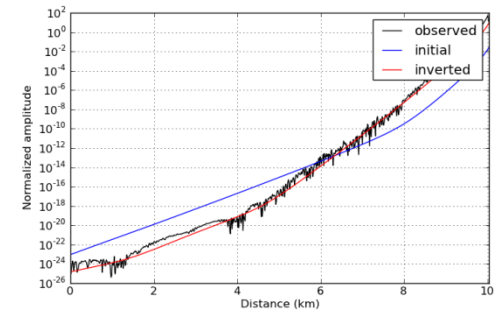
(c)



(d)

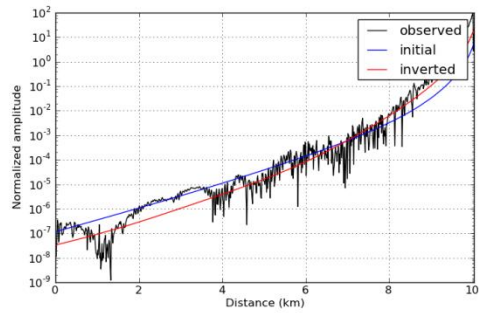


(e)

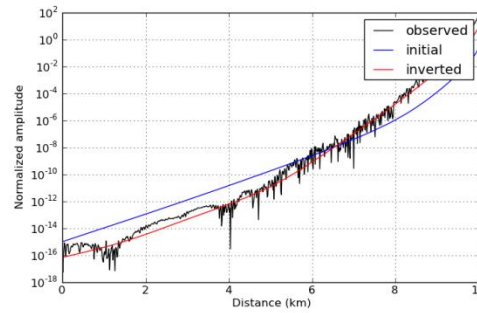


(f)

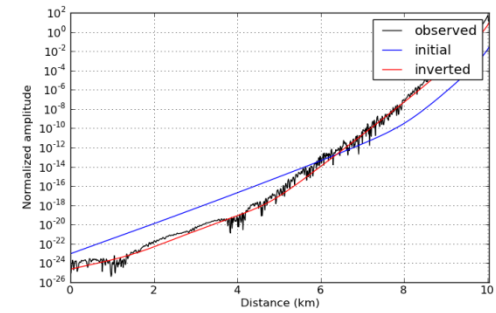
Figure 42. Comparison of the Laplace-domain observed and modeled data at the 601st shot position using the conventional LWI result with damping constants of (a) 3, (b) 7, and (c) 11 s⁻¹. (d), (e), and (f) are the same comparison as (a), (b), and (c) using the single-damping LWI result



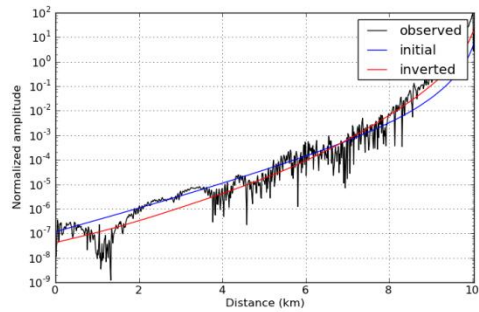
(a)



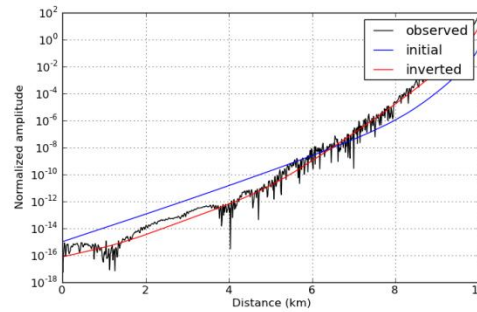
(b)



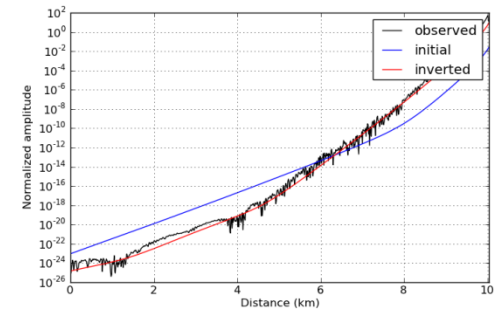
(c)



(d)



(e)



(f)

Figure 43. Comparison of the Laplace-domain observed and modeled data at the 901st shot position using the conventional LWI result with damping constants of (a) 3, (b) 7, and (c) 11 s^{-1} . (d), (e), and (f) are the same comparison as (a), (b), and (c) using the single-damping LWI result

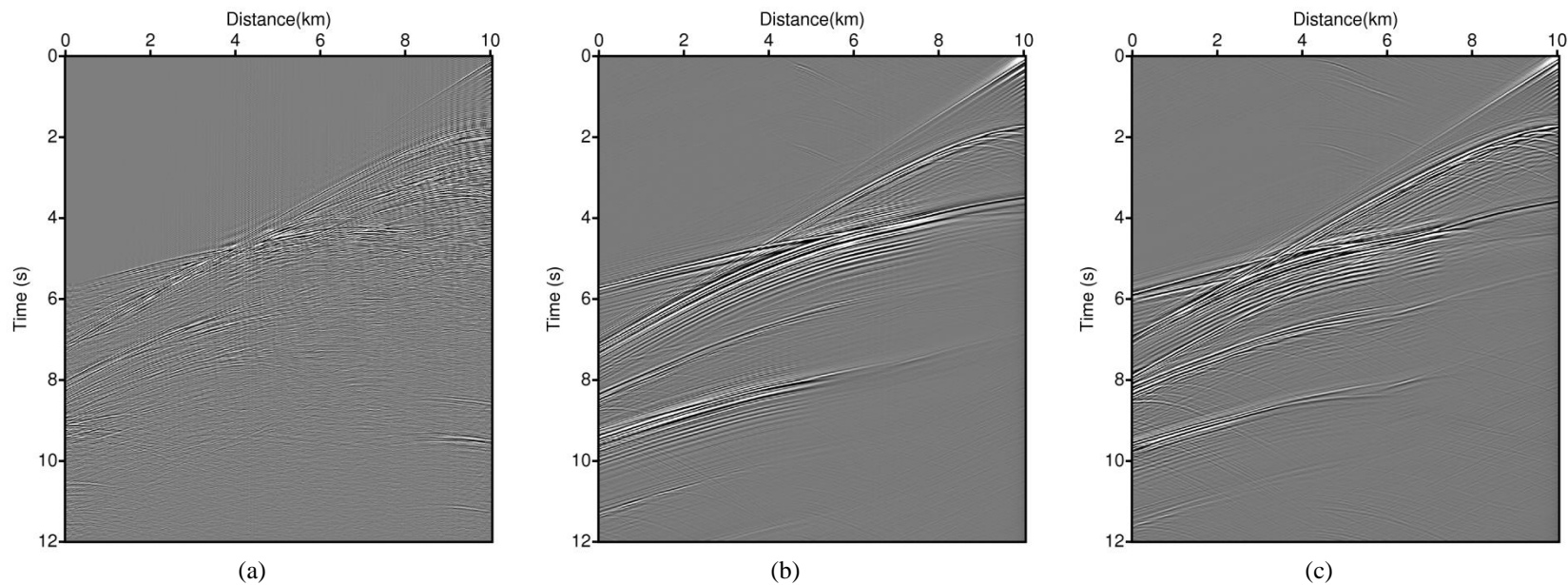


Figure 44. Time-domain (a) observed data and modeled data using the result of (b) conventional LWI and (c) single-damping LWI at the 301st shot position

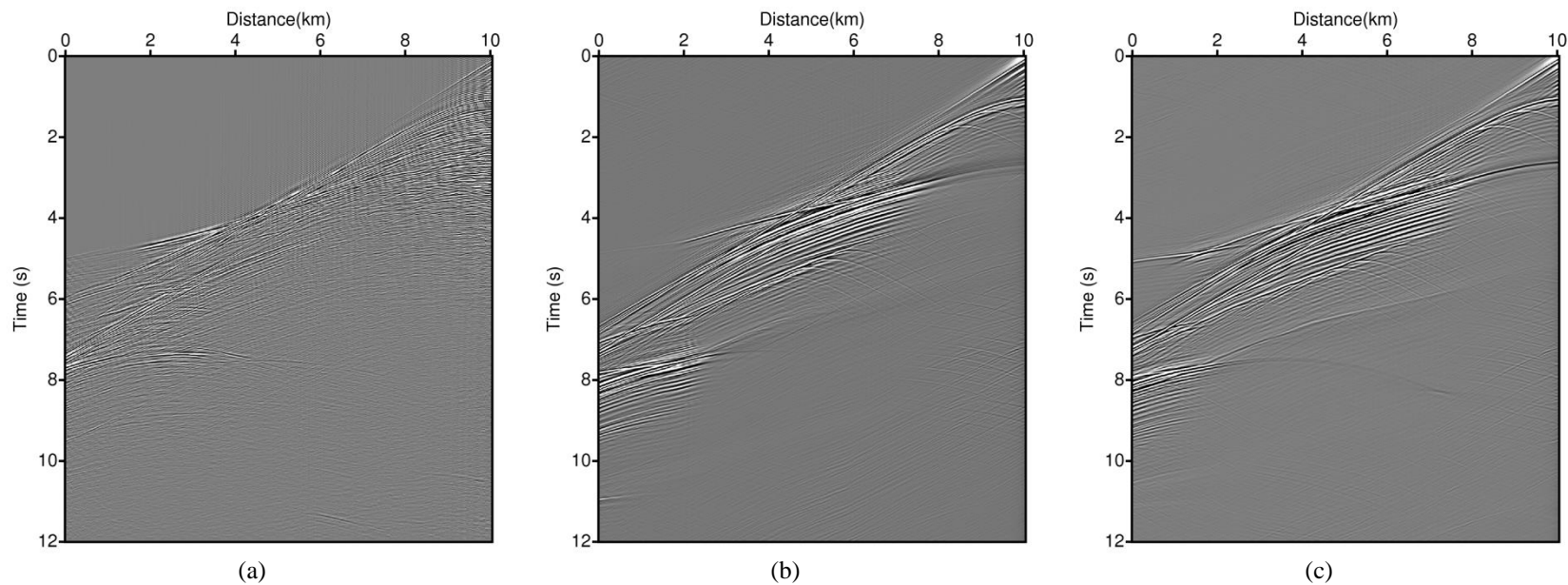


Figure 45. Time-domain (a) observed data and modeled data using the result of (b) conventional LWI and (c) single-damping LWI at the 601st shot position

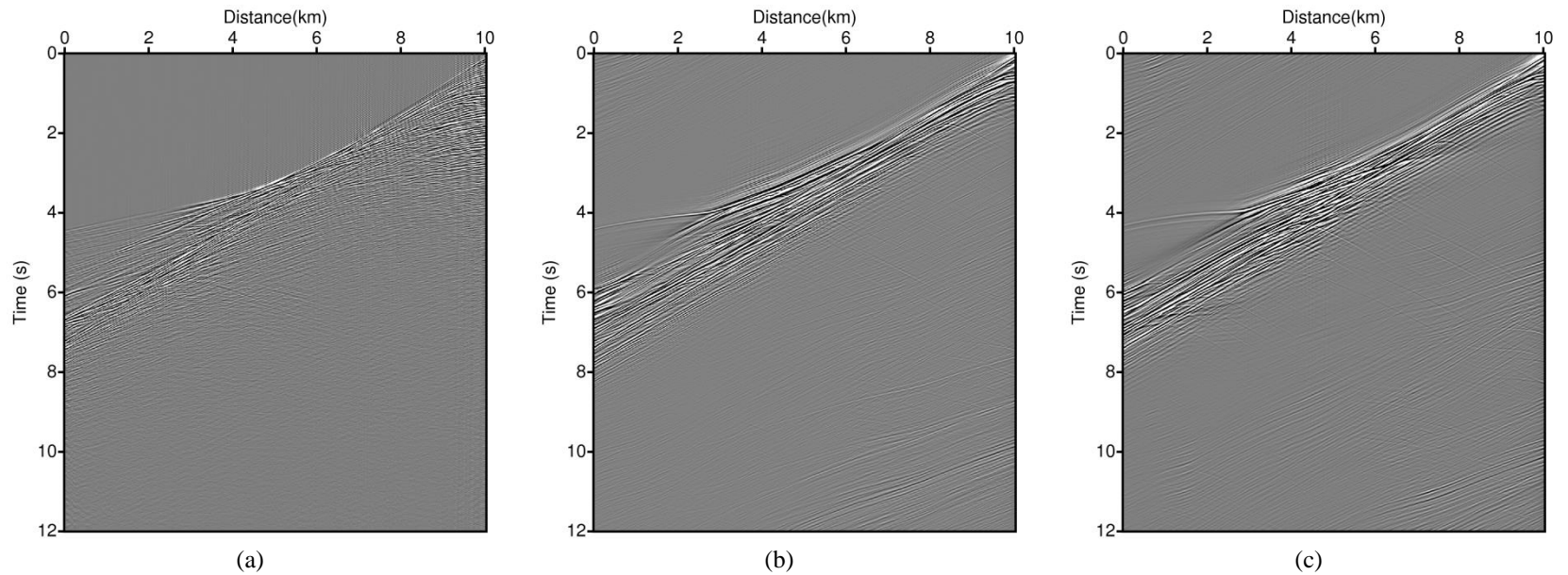


Figure 46. Time-domain (a) observed data and modeled data using the result of (b) conventional LWI and (c) single-damping LWI at the 901st shot position

5. Conclusion

LWI is an innovative waveform inversion algorithm for producing long-wavelength velocity models using seismic data lacking low-frequency information. Since the initial version of the LWI algorithm using an acoustic approximation was developed in 2008, the algorithm has been extended in various directions (e.g., elastic waveform inversion, 3-D media waveform inversion, and LWI using time-domain modeling), and it has been applied to various synthetic and real datasets. In those studies, selecting and grouping the optimal damping constants are two of the most important stages. However, most studies use several damping constants that are selected empirically without investigating the role of each damping constant and potential issues caused by certain damping constants.

This study is motivated by the fact that the wave propagation and constructed gradient directions using different damping constants in the Laplace domain are analogous to each other. In this study, I propose that inverting the wave field for one of the representative damping constants produces comparable results to conventional LWI while greatly reducing the computing costs. In addition, when considering more realistic seismic data, I expect that several problems can appear while inverting the wave field for relatively small and large damping constants, and they are analyzed mathematically and verified with numerical examples. New scaling method using depth weighting function, which scales the gradient obtained by a single damping constant, is introduced to enhance the quality of the inversion result. Based on the numerical test using synthetic data obtained from the Pluto 1.5 velocity model, I suggest that a damping constant should be selected among the various damping constants ranging from 5 to 9 s^{-1} for a single-damping LWI algorithm. The computational efficiency of the proposed single-damping LWI is enhanced up to 6 times in the synthetic data example compared to the conventional LWI using 7 damping constants while maintaining the quality of the inversion result. As well as the synthetic dataset, a real dataset, which is

acquired from a deep-sea environment with high-velocity salt structures, are also used to verify the proposed algorithm, and the inverted velocity model obtained by single-damping LWI shows similar results when it is compared with that of conventional LWI. The migrated images from the reverse-time migration algorithm, and Laplace- and time-domain simulated wave fields are also identical to each other for both inverted velocity models.

In spite of the successful application of the proposed single-damping LWI for both synthetic and real data, a seismic dataset acquired from an environment with different geological features has to be used to investigate the robustness of the proposed algorithm in future studies. Mostly, LWI is followed by Laplace-Fourier-domain waveform inversion (LFWI) and frequency-domain waveform inversion to introduce more detailed velocity structures into the background smooth velocity model. As in the single-damping LWI, selecting a single representative damping constant for LFWI can be studied in future studies.

Reference

- Amunson, L., 1991. Comparison of the least-squares criterion and the Cauchy criterion in frequency-wavenumber inversion. *Geophysics* 56, 2027–2035.
- Bae, H.S., Pyun, S., Shin, C., Marfurt, K.J., Chung, W., 2012. Laplace-domain waveform inversion versus refraction-traveltime tomography. *Geophys. J. Int.* 190, 595–606. doi:10.1111/j.1365-246X.2012.05504.x
- Baysal, E., Kosloff, D.D., Sherwood, J.W.C., 1983. Reverse time migration. *Geophysics* 48, 1514–1524.
- Billette, F., Bégat, S. Le, Podvin, P., Lambaré, G., 2003. Practical aspects and applications of 2D stereotomography. *Geophysics* 68, 1008. doi:10.1190/1.1581072
- Billette, F., Lambaré, G., 1998. Velocity macro-model estimation from seismic reflection data by stereotomography. *Geophys. J. Int.* 135, 671–690. doi:10.1046/j.1365-246X.1998.00632.x
- Bunks, C., Saleck, F.M., Zaleski, S., Chavent, G., 1995. Multiscale seismic waveform inversion. *Geophysics* 60, 1457–1473.
- Cruse, E., Pica, A., Noble, M., McDonald, J., Tarantola, A., 1990. Robust elastic nonlinear waveform inversion: Application to real data. *Geophysics* 55, 527–538.
- Golub, G.H., Loan, C.F. Van, 1996. *Matrix computations*, 3rd ed. Johns Hopkins University Press.
- Guitton, A., Symes, W.W., 2003. Robust inversion of seismic data using the Huber norm. *Geophysics* 68, 1310. doi:10.1190/1.1598124
- Ha, T., Chung, W., Shin, C., 2009. Waveform inversion using a back-propagation algorithm and a Huber function norm. *Geophysics* 74, R15. doi:10.1190/1.3112572
- Ha, W., Cha, Y., Shin, C., 2010a. A comparison between Laplace domain and frequency domain methods for inverting seismic waveforms. *Explor. Geophys.* 41, 189–197. doi:10.1071/EG09031
- Ha, W., Chung, W., Park, E., Shin, C., 2012a. 2-D acoustic Laplace-domain waveform inversion of marine field data. *Geophys. J. Int.* 190, 421–428. doi:10.1111/j.1365-246X.2012.05487.x

- Ha, W., Chung, W., Shin, C., 2012b. Pseudo-Hessian matrix for the logarithmic objective function in full waveform inversion. *J. Seism. Explor.* 21, 201–214.
- Ha, W., Pyun, S., Yoo, J., Shin, C., 2010b. Acoustic full waveform inversion of synthetic land and marine data in the Laplace domain. *Geophys. Prospect.* 58, 1033–1048. doi:10.1111/j.1365-2478.2010.00884.x
- Ha, W., Shin, C., 2013. Why do Laplace-domain waveform inversions yield long-wavelength results? *Geophysics* 78, R167–R173. doi:10.1190/geo2012-0365.1
- Ha, W., Shin, C., 2012a. Efficient full waveform inversion using a cyclic shot sampling method, in: *SEG Technical Program Expanded Abstracts*. pp. 1–5. doi:10.1190/segam2012-0560.1
- Ha, W., Shin, C., 2012b. Laplace-domain full-waveform inversion of seismic data lacking low-frequency information. *Geophysics* 77, R199. doi:10.1190/geo2011-0411.1
- Kim, J.H., Kim, S.J., 1999. Multifrontal solver combined with graph partitioners. *AIAA J.* 37, 964–970. doi:10.2514/3.14270
- Kim, Y., Cha, Y.H., Shin, C., Ko, S., Seo, Y., 2009. Improved logarithmic waveform inversion considering the power-spectrum of the wavefield. *J. Seism. Explor.* 18, 215–228.
- Kim, Y., Cho, H., Min, D.-J., Shin, C., 2011a. Comparison of frequency-selection strategies for 2D frequency-domain acoustic waveform inversion. *Pure Appl. Geophys.* 168, 1715–1727. doi:10.1007/s00024-010-0196-8
- Kim, Y., Min, D.-J., Shin, C., 2011b. Frequency-domain reverse-time migration with source estimation. *Geophysics* 76, S41. doi:10.1190/1.3534831
- Kim, Y., Shin, C., Calandra, H., Min, D.-J., 2013. An algorithm for 3D acoustic time-Laplace-Fourier-domain hybrid full waveform inversion. *Geophysics* 78, R151–R166. doi:10.1190/geo2012-0155.1
- Koo, N.H., Shin, C., Min, D.-J., Park, K.-P., Lee, H.Y., 2011. Source estimation and direct wave reconstruction in Laplace-domain waveform inversion for deep-sea seismic data. *Geophys. J. Int.* 187, 861–870. doi:10.1111/j.1365-246X.2011.05141.x

- Lailly, P., 1983. The seismic inverse problem as a sequence of before stack migrations, in: Conference on Inverse Scattering, Theory and Applications, SIAM. pp. 206–220.
- Li, Y., Oldenburg, D.W., 1998. 3-D inversion of gravity data. *Geophysics* 63, 109. doi:10.1190/1.1444302
- Li, Y., Oldenburg, D.W., 1996. 3-D inversion of magnetic data. *Geophysics* 61, 394. doi:10.1190/1.1443968
- Marfurt, K.J., 1984. Accuracy of finite-difference and finite-element modeling of the scalar and elastic wave equations. *Geophysics* 49, 533–549.
- McMECHAN, G. a., 1983. Migration By Extrapolation of Time-Dependent Boundary Values. *Geophys. Prospect.* 31, 413–420. doi:10.1111/j.1365-2478.1983.tb01060.x
- Mora, P., 1987. Nonlinear two-dimensional elastic inversion of multioffset seismic data. *Geophysics* 52, 1211–1228.
- Operto, S., Ravaut, C., Imbrota, L., Virieux, J., Herrero, a., Dell’Aversana, P., 2004. Quantitative imaging of complex structures from dense wide-aperture seismic data by multiscale traveltime and waveform inversions: A case study. *Geophys. Prospect.* 52, 625–651. doi:10.1111/j.1365-2478.2004.00452.x
- Plessix, R., 2006. A review of the adjoint-state method for computing the gradient of a functional with geophysical applications. *Geophys. J. Int.* 167, 495–503. doi:10.1111/j.1365-246X.2006.02978.x
- Plessix, R., Baeten, G., 2010. Application of acoustic full waveform inversion to a low-frequency large-offset land data set, in: SEG Technical Program Expanded Abstracts. pp. 930–934. doi:10.1190/1.3513930
- Pratt, R.G., Shin, C., Hicks, G.J., 1998. Gauss-Newton and full Newton methods in frequency domain seismic waveform inversion. *Geophys. J. Int.* 133, 341–362.
- Prieux, V., Brossier, R., Operto, S., Virieux, J., 2013. Multiparameter full waveform inversion of multicomponent ocean-bottom-cable data from thevalhall field. part 1: Imaging compressional wave speed, density and attenuation. *Geophys. J. Int.* 194, 1640–1664. doi:10.1093/gji/ggt177
- Pyun, S., Son, W., Shin, C., 2011. 3D acoustic waveform inversion in the Laplace domain using an iterative solver. *Geophys. Prospect.* 59, 386–399. doi:10.1111/j.1365-2478.2010.00927.x

- Shin, C., Cha, Y.H., 2009. Waveform inversion in the Laplace-Fourier domain. *Geophys. J. Int.* 177, 1067–1079. doi:10.1111/j.1365-246X.2009.04102.x
- Shin, C., Cha, Y.H., 2008. Waveform inversion in the Laplace domain. *Geophys. J. Int.* 173, 922–931. doi:10.1111/j.1365-246X.2008.03768.x
- Shin, C., Ha, W., 2008. A comparison between the behavior of objective functions for waveform inversion in the frequency and Laplace domains. *Geophysics* 73, VE119. doi:10.1190/1.2953978
- Shin, C., Jang, S., Min, D.-J., 2001. Improved amplitude preservation for prestack depth migration by inverse scattering theory. *Geophys. Prospect.* 49, 592–606. doi:10.1046/j.1365-2478.2001.00279.x
- Shin, C., Koo, N.H., Cha, Y.H., Park, K.-P., 2010. Sequentially ordered single-frequency 2-D acoustic waveform inversion in the Laplace-Fourier domain. *Geophys. J. Int.* 181, 935–950. doi:10.1111/j.1365-246X.2010.04540.x
- Shin, C., Min, D.-J., 2006. Waveform inversion using a logarithmic wavefield. *Geophysics* 71, R31. doi:10.1190/1.2194523
- Shin, C., Pyun, S., Bednar, J.B., 2007. Comparison of waveform inversion , part1 : conventional wave field vs logarithmic wave field. *Geophys. Prospect.* 55, 449–464.
- Shin, J., Ha, W., Jun, H., Min, D.-J., Shin, C., 2014. 3D Laplace-domain full waveform inversion using a single GPU card. *Comput. Geosci.* 67, 1–13. doi:10.1016/j.cageo.2014.02.006
- Shin, J., Kim, Y., Shin, C., Calandra, H., 2013. Laplace-domain full waveform inversion using irregular finite elements for complex foothill environments. *J. Appl. Geophys.* 96, 67–76. doi:10.1016/j.jappgeo.2013.06.008
- Shipp, R.M., Singh, S.C., 2002. Two-dimensional full wavefield inversion of wide-aperture marine seismic streamer data. *Geophys. J. Int.* 151, 325–344. doi:10.1046/j.1365-246X.2002.01645.x
- Sirgue, L., Pratt, R.G., 2004. Efficient waveform inversion and imaging: A strategy for selecting temporal frequencies. *Geophysics* 69, 231. doi:10.1190/1.1649391
- Soubaras, R., Lafet, Y., 2013. Variable-depth streamer acquisition: Broadband data for imaging and inversion. *Geophysics* 78, WA27–WA39. doi:10.1190/1.3627683

- Symes, W.W., 2008. Migration velocity analysis and waveform inversion. *Geophys. Prospect.* 56, 765–790. doi:10.1111/j.1365-2478.2008.00698.x
- Symes, W.W., Carazzone, J.J., 1991. Velocity inversion by differential semblance optimization. *Geophysics* 56, 654–663.
- Tarantola, A., 1986. A strategy for nonlinear elastic inversion of seismic reflection data. *Geophysics* 51, 1893–1903.
- Tarantola, A., 1984. Inversion of seismic reflection data in the acoustic approximation. *Geophysics* 49, 1259–1266.
- Toomey, D.R., Solomon, S.C., Purdy, G.M., 1994. Tomographic imaging of the shallow crustal structure of the East Pacific Rise at 9°30'N. *J. Geophys. Res.* 99, 24,135–24,157.
- Virieux, J., Operto, S., 2009. An overview of full-waveform inversion in exploration geophysics. *Geophysics* 74, WCC1. doi:10.1190/1.3238367
- Whitmore, N.D., 1983. Iterative Depth Migration by Backward Time Propagation, in: *SEG Technical Program Expanded Abstracts*. pp. 382–385.
- Yang, T., Sava, P., 2011. Wave-equation migration velocity analysis with time-shift imaging. *Geophys. Prospect.* 59, 635–650. doi:10.1111/j.1365-2478.2011.00954.x
- Yilmaz, O., 1987. *Seismic Data Analysis*. SEG Books.
- Yilmaz, O., Chambers, R., 1984. Migration velocity analysis by wave-field extrapolation. *Geophysics* 49, 1664–1674.
- Zauderer, E., 2006. *Partial Differential Equations of Applied Mathematics*, 3rd ed. Wiley.
- Zelt, C.A., Barton, P.J., 1998. Three-dimensional seismic refraction tomography: A comparison of two methods applied to data from the Faeroe Basin. *J. Geophys. Res.* 103, 7187. doi:10.1029/97JB03536

초록

단일 감쇠상수를 이용한 라플라스 영역 완전파형역산

신 정 균

에너지시스템공학부

서울대학교 대학원

라플라스 영역 완전파형역산은 라플라스 변환된 파동장을 이용하여 지하매질의 장파장 속도모델을 구축하는 지하구조 영상화 기술이다. 라플라스 영역 완전파형역산은 유의미한 저 주파수 성분이 부재한 현장자료에 대해서 최소화된 전처리 과정 이후 인간의 주관적인 판단 없이 자동적으로 장파장 속도모델을 구축할 수 있다는 점에서 전 세계의 산업계와 학계로부터 인정을 받았다. 최근에는 불규칙한 표면을 가진 매질 혹은 3차원 음향 매질, 3차원 탄성 매질, 3차원 음향-탄성 결합 매질 등 좀더 현실적인 환경에 대해서 기술의 확장이 이루어지고 있는 추세이다. 더불어 그래픽 처리장치를 이용한 시간 영역 모델링 혹은 반복 행렬 풀이법을 이용한 모델링 등을 활용하여 라플라스 영역 완전파형역산의 계산 효율성 또한 크게 향상되고 있다. 현재까지 개발된 라플라스 영역 완전파형역산은 다양한 감쇠상수의 조합을 통해서 얻어진 최대 경사방향을 중첩하여 이를 반복적으로 업데이트함으로써 수행 되었고, 많은 인공합성 자료와 현장 자료에 대해서 유의미한 결과를 도출하였다. 하지만, 각각의 감쇠상수가 가지는 역할은 명확하게 밝혀지지 않았고 다양한 감쇠상수의 조합 또한 이론적 근거에 기반을 두지 않은 채 순수한 경험에 의존하고 있었다. 게다가 극단적으로 작은 감쇠상수 혹은 큰 감쇠상수가 가지는 잠재적인 문제점에 대해서도 심도 깊은 연구가 이루어지지 않았고, 다수의 감쇠상수들의 사용에 따른 컴퓨터 계산의 효율성 저하의 문제를 안고 있었다.

이번 연구의 주제인 단일 감쇠상수를 이용한 라플라스 영역 파형역산은 서로 다른 감쇠상수들이 만들어내는 역산결과의 유사성에서 영감을 받

이 연구가 이루어졌다. 본 연구에서는 인공합성 자료를 이용한 수치 실험을 통하여 다양한 감쇠상수들의 역할에 대해서 정성적인 분석이 이루어졌으며 작은 감쇠상수와 큰 감쇠상수가 만들어 내는 잠재적인 문제점에 대한 수학적 접근이 이루어졌다. 이를 통해 단일 감쇠상수를 이용한 라플라스 영역 완전 파형역산에 사용될 수 있는 적절한 감쇠상수의 범위를 제시하였고 이들 중 하나의 감쇠상수를 선택함으로써 역산결과의 질을 유지함과 동시에 이에 필요한 컴퓨터 계산을 크게 절약할 수 있었다. 심도 가중 함수를 활용한 스케일링이 제시되었고 이는 단일 감쇠상수를 이용한 라플라스 영역 파형역산의 수렴성을 향상시켰다. 마지막으로 해양 환경에서 얻어진 현장 자료를 이용하여 제시된 알고리즘이 검증되었다.

주요어 : 라플라스 영역 파형역산, 완전 파형역산, 단일 감쇠 상수, 심도 가중 함수

학번 : 2011-21101